Assessing synergistic radar and radiometer capability in retrieving ice cloud microphysics based on hybrid Bayesian algorithms

Yuli Liu[1], **Gerald G. Mace**[1]

[1]University of Utah

Key Points:

- We develop hybrid Bayesian algorithms for synergistic radar and radiometer retrievals of ice cloud microphysics
- The algorithms combine Bayesian Monte Carlo Integration and different optimization methods to retrieve quantities and uncertainty estimations
- We conduct simulated experiments to quantitively assess the objective remote sensors capability in ice cloud remote sensing

Corresponding author: Yuli Liu, yuli.liu@utah.edu

Abstract

The 2017 National Academy of Sciences Decadal Survey highlighted several high priority objectives to be pursued during the next decadal timeframe, and the next-generation Cloud Convection Precipitation (CCP) observing system is thereby contemplated. In this study, we investigate the capability for ice cloud remote sensing of two CCP candidate observing systems that include a W-band cloud radar and a submillimeter-wave radiometer by developing hybrid Bayesian algorithms for the active-only, passive-only, and synergistic retrievals. The hybrid Bayesian algorithms combine the Bayesian MCI and optimization process to retrieve quantities and uncertainty estimates. The radar-only retrievals employ an optimal estimation methodology, while the radiometer-involved retrievals employ ensemble approaches to maximize the posterior probability density function. The a priori information is obtained from the Tropical Composition, Cloud and Climate Coupling (TC4) in situ data and CloudSat radar observations. Simulation experiments are conducted to evaluate the retrieval accuracies by comparing the retrieved parameters with the known values. The experiment results suggest that the radiometer measurements provide little information on the vertical distributions of ice cloud microphysics. Radar observations have better capacity for retrieving water content compared to particle number concentration. The synergistic information is demonstrated to be helpful in improving retrieval accuracies, especially for the ice water path retrievals. The end-to-end simulation experiments also provide a framework that could be extended to the inclusion of other remote sensors to further assess the CCP observing system in future studies.

1 Introduction

The 2017 earth science decadal survey (Board et al., 2019) identified five designated foundational observations to be pursued during the 2017-2027 time frame, and the Aerosols (A), and Clouds, Convection, and Precipitation (CCP) are included as designated observables (DOs). In the preformulation study, the A and CCP DOs were merged to exploit synergies in the measurement systems. The objective of the preformulation study was to identify measurables that can achieve the science objectives of the DOs. As such, the study identified observing system architectures that maximize science benefit while limiting cost and risk. To narrow in on a set of viable architectures, the ACCP study relied on a suite of Observing System Simulation Experiments (OSSEs) aimed at addressing pixel-level retrieval uncertainties and sampling trade-offs for various geophysical variables that were deemed important to achieving science goals.

The properties of ice clouds are among the critical geophysical variables in the CCP science objectives. Ice clouds play a significant role in modulating the energy budget of the earth system by absorbing upwelling long-wave radiation emitted from the lower troposphere and reflecting incoming solar short-wave radiation (Liou, 1986; Su et al., 2017). Studies suggest that ice clouds are a net heat source to the climate system (Stephens & Webster, 1984; Berry & Mace, 2014) while contributing a positive feedback to the climate system (Zelinka & Hartmann, 2011).

The radiative effects of ice clouds depend on the vertically integrated and the vertical distribution of ice particle characteristics (Ackerman et al., 1988; Hartmann & Berry, 2017). Microwave RAdio Detection And Ranging (RADAR) and the submillimeter-wave radiometry are two critical techniques for ice cloud remote sensing that are strongly synergistic when combined (Buehler et al., 2012). The microwave radar provides radar reflectivity that constrain ice cloud microphysical quantities in a vertically resolved sense while the submillimeter-wave radiometer constrains integrated mass and particle size. These two techniques are also highly complementary. The nadir looking microwave cloud radar provides high resolution of ice cloud vertical profiles but are limited to the along-track measurements, whereas the scanning submillimeter-wave radiometer has a wide

swath but provides limited information about cloud vertical structure. Combing the strength of both observing sensors enhances our capability to better acquire ice cloud spatial distributions.

Several retrieval algorithms have been developed specifically for ice cloud radiometry studies. All applicable algorithms that could be roughly classified as statistical approaches and optimization approaches are under the framework of Bayes theorem. The statistical approaches, including the Bayesian Monte Carlo Integration (MCI) (Evans et al., 2002, 2005) and the Neural Network (Jimenez et al., 2007; Brath et al., 2018), builds up an a priori database by randomly generating atmospheric/cloud cases according to a prior probability density function (PDF) and simulating instrument-specific measurements. The retrieval results are obtained through interpolation over the precalculated databases. To solve the sparsity of database cases in the measurement space, optimization algorithms are developed to maximize the posterior PDF. Evans et al. (2012) applied the Optimal Estimation Method (OEM) and Markov Chain Monte Carlo (MCMC) to retrieve ice cloud profiles from the Compact Scanning Submillimeter Imaging Radiometer (CoSSIR; (Evans et al., 2005)) observations during the Tropical Composition, Cloud and Climate Coupling (TC4; (Toon et al., 2010)) experiment. Liu et al. (2018) proposed an ensemble estimation algorithm that does not use the gradient information but always relies on estimating posterior PDF to minimize the cost function. For the combined radar and radiometer retrievals, Pfreundschuh et al. (2020) developed OEM algorithms for the upcoming Ice Cloud Imager radiometer (Kangas et al., 2014) and a conceptual W-band cloud radar to investigate to synergies between the active and passive observations.

The objective of this paper is to develop candidate algorithms for synergistic radar and radiometer retrievals to quantitively assess the capability of sensing designated ice cloud geophysical variables for the next-generation ACCP observing system. The algorithms for active-only, passive-only, and combined retrievals use a hybrid Bayesian framework, which combines the Bayesian MCI and optimization process to retrieve ice cloud quantities with uncertainty estimates. This paper is structured as follows: Section 2 describes the objective submillimeter-wave radiometer and the reference cloud sense used for testing the retrieval accuracies; Section 3 describes the hybrid Bayesian algorithms for the radar-only, radiometer-only, and synergistic retrievals in detail; Section 4 describes the a priori database that is derived from in situ data and CloudSat Cloud Profiling Radar observations; Section 5 conducts the retrieval simulation experiments and quantitively evaluates the retrieval performance; and finally, Section 6 presents the summaries and conclusions.

2 Simulated observations

2.1 remote sensors

The remote sensors we evaluate in this study include a W-Band radar and a (sub)millimeter wave radiometer both of which are candidates in the ACCP observing system. The W-band cloud radar that we assume here is similar to the Cloud Profiling Radar (CPR) in the CloudSat satellite (Stephens et al., 2008; Tanelli et al., 2008). The passive radiometer we consider is conical-scanning with 16 horizontally polarized channels at the frequencies of 118 1.1, 118 1.5, 118 2, 118 5, 183 1, 183 2, 183 3, 183 6, 240, 310, 380 0.75, 380 1.5, 380 3, 380 6, 660, and 880 GHz. Most frequency channels are centered on water vapor absorption lines. This radiometer has a 45 off-nadir angle and a 750 km swath width. Figure 1 shows the simulated clear-sky brightness temperature (BT) spectrum for a tropical atmospheric scenario. All passive sensors channel positions and a detailed view of the double sidebands located on either side of a central frequency are shown.

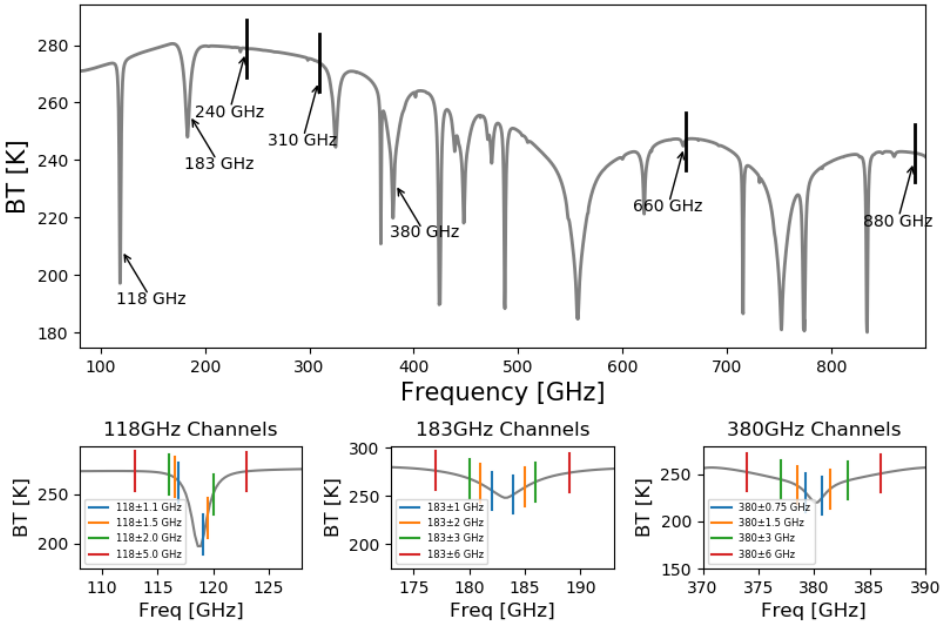

Figure 1. Simulated clear-sky brightness temperature spectrum at a tropical atmospheric scenario. All ACCP radiometer channel positions and a detailed view of the double sidebands located on either side of a central frequency are present.

2.2 reference cloud scenes

The major consideration in selecting reference cloud scenes is to guarantee its independence with the cloud microphysics in the a priori retrieval database (see more details in Section 4.2), but also to keep the two datasets consistent in a geographic context. In this study, we select cloud profiles along a tropical transect that are simulated using the Environment and Climate Change Canada (ECCC) model (Chen et al., 2018) and those profiles were made available to the ACCP Science Impacts Team (Kollias, personal communication). The model outputs provide the water content and number concentration for cloud ice, snow, liquid cloud, and rain, but only frozen cloud particles (ice and snow) are used in this study since only ice cloud vertical profiles are presently synthesized in the a priori database (refer to Section 4.2 for more details). In the numerical models, cloud ice is generally characterized by high particle number densities and small particle sizes, while snow is characterized by lower number densities and larger particle size. The model outputs have a vertical resolution of 100-meter, but all atmospheric profiles and microphysical cloud parameters are interpolated according to a range gate spacing similar to CloudSat. We select a transect among the ECCC mode outputs which covers the region between -2.5 and 9 latitude. The selected cloud scenes for testing contain 1280 atmosphere/cloud profiles in total.

We develop the forward model for both active and passive simulations based on the Atmospheric Radiative Transfer Simulator (Buehler et al., 2005; Eriksson et al., 2011). ARTS is dedicated to radiative transfer calculations in the millimeter and submillimeter spectral range. The recently published Single Scattering Databases (SSD) for total random orientation (Eriksson et al., 2018) and azimuthal random orientation (Brath et al., 2020) make it more powerful in investigating various ice cloud properties. The ARTS

forward model developed in this study employs the two-moment scheme that requires both water content and number concentration as input to describe the particle size distribution (PSD). The frozen particles are assumed to be randomly orientated, and the scattering properties for both ice and snow are approximated by the EvansSnow habit from the ARTS SSD database. The forward model used during the optimization process applies the same particle habit since the uncertainties introduced by various particle habits are not investigated in this study.

Figure 2 shows the vertical distribution of water content and number concentration for cloud ice and snow particles along the selected latitudinal transact and the corresponding W-band radar simulations. The radar minimum sensitivity is set to be -30 dBz, thus some thin clouds are not detected. Compared to the number concentration, the radar simulations show more tendency to follow the variation of IWC. Figure 3 shows the IWP and the corresponding BT simulations for all ACCP radiometer channels. A clear relationship between the IWP and BT depression is evident. The channels with higher central frequency are more sensitive to the change of water path. For the double sidebands centered on the same center frequency, the large frequency-offset channels show higher brightness temperature values in clear sky conditions, and they have larger BT depressions when encountering thick ice cloud layers.

Figure 4 shows the scatterplot of the BT difference between simulations in the clear sky and cloudy conditions versus IWP for different channels. The 118 GHz channels demonstrate sensitivity when the IWP is over $10^3 \mathrm{g/m}^2$. This is not surprising since the 118 GHz channels are primely designed for sensing temperature profiles. For the 183 GHz and 380 GHz channels, the biggest BT differences are up to 50 K and 80 K, respectively. Also, the 380 GHz channels simulations show more separation for the same IWP values, implying that the high-frequency channels are more sensitive to the IWC vertical distributions. The BT difference for the 660 GHz and 880GHz window channels are noticeable even when the IWP is below 100 g/m^2, and the difference values could up to 110 K under our reference cloud sense. These two channels make the ACCP radiometer capable of sensing thin clouds that are usually composed of small particles. However, both 660 and 880 GHz show signs of saturation for IWP in excess of $10^3 \mathrm{g/m}^2$.

3 Hybrid Bayesian algorithms

We developed different hybrid Bayesian algorithms for the radar-only, radiometer-only, and synergistic retrievals of ice cloud parameters from the reference cloud scenes. All hybrid algorithms combine Bayesian MCI with optimization processes to retrieve quantities and uncertainty estimates. Bayesian MCI introduces the prior information by generating an ensemble of atmospheric cases that are distributed according to the prior PDF to build up the retrieval database, which is highly efficient since the retrievals are done by interpolating the database cases and no more forward model calculations are required. By assuming the uncertainties for different measurement variables to be independent, the conditional PDF, which is also the posterior PDF, can be written as:

$$p_{cond}(x|y_{obs}) \propto exp(-\frac{1}{2}\chi^2) \qquad \chi^2 = \sum_{j=1}^{M} \frac{(y_{sim,j} - y_{obs,j})^2}{\sigma_j^2} \tag{1}$$

where p_{cond} is the conditional probability of the measurement vector y_{obs} given a particular atmospheric state x, y_{sim} is the simulated observation vector, and σ_j^2 is the uncertainty of observation and forward model. The retrieved quantities and uncertainties are calculated by Monte Carlo Integration over the state vectors to find the mean vec-

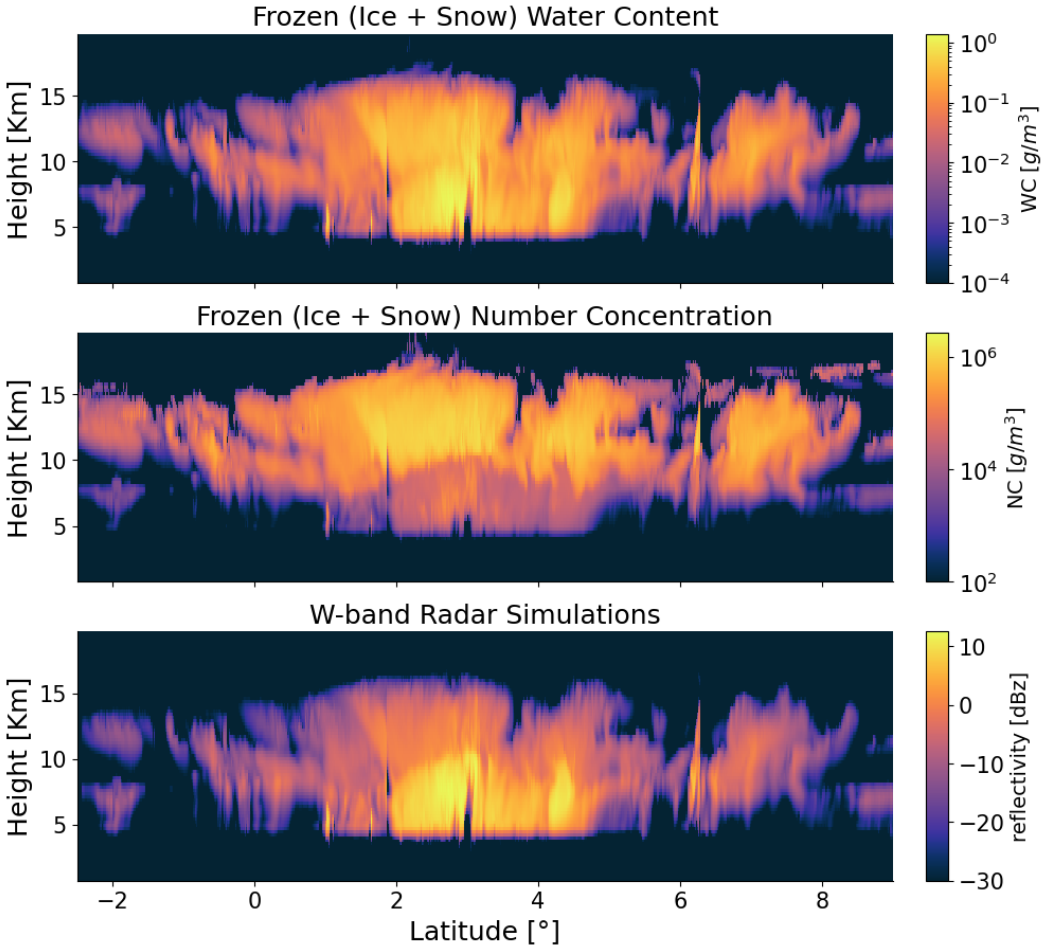

Figure 2. Vertical distribution of water content (WC) and number concentration (NC) for ice and snow particles along the selected latitudinal transact and the corresponding W-band radar reflectivity simulations. The radar simulations are computed using Atmospheric Radiative Transfer Simulator (ARTS) forward model.

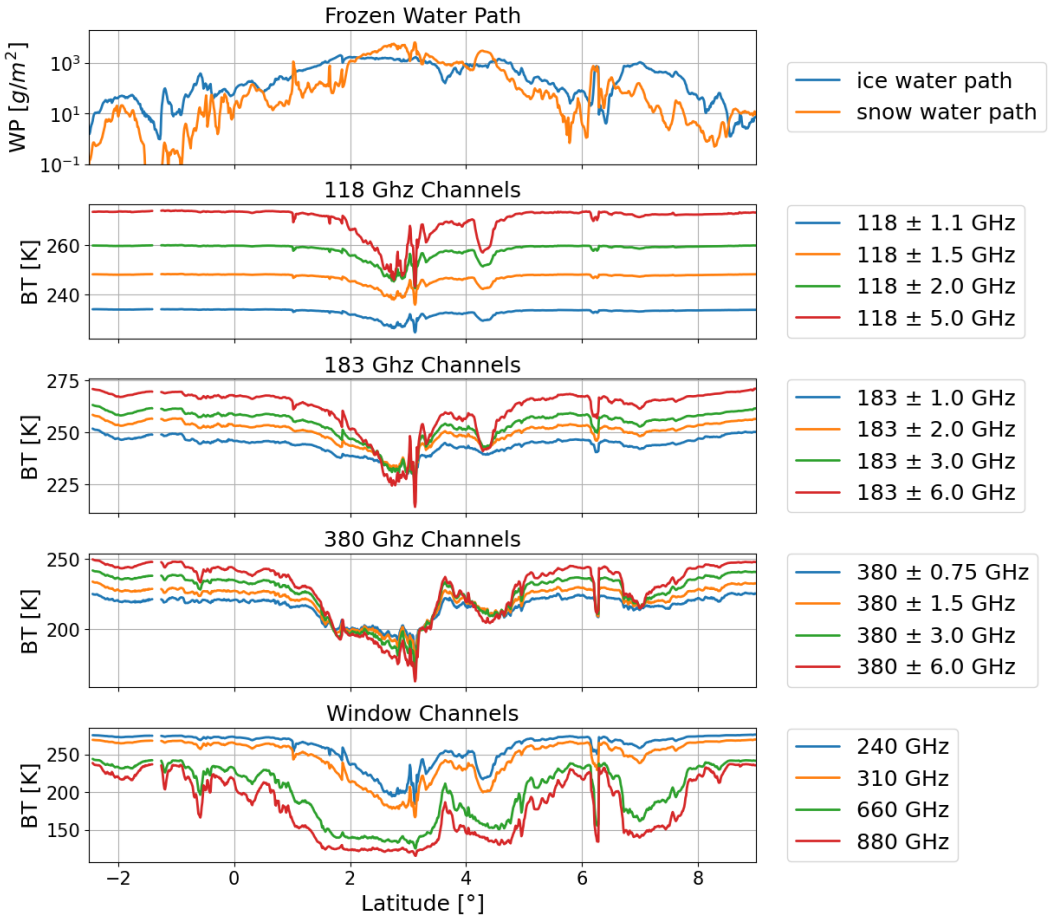

Figure 3. Integrated water content for ice and snow particles for the selected latitudinal transect and the corresponding brightness temperature simulations for all ACCP radiometer channels.

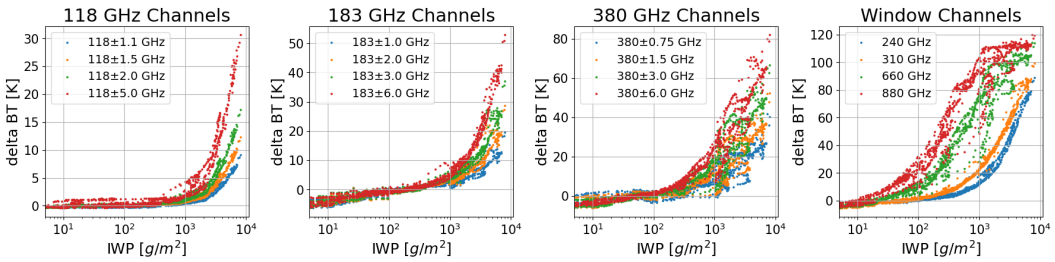

Figure 4. Scatterplot of the brightness temperature difference between simulations in the clear sky and cloudy conditions as a function of ice water path for all ACCP radiometer channels.

tor and the associated standard deviation:

$$\bar{x} = \frac{\sum_i x_i exp(-\frac{1}{2}\chi_i^2)}{\sum_i exp(-\frac{1}{2}\chi_i^2)}$$
$$\sigma_{\bar{x}} = \sqrt{\frac{\sum_i (x_i - \bar{x})^2 exp(-\frac{1}{2}\chi_i^2)}{\sum_i exp(-\frac{1}{2}\chi_i^2)}} \quad (2)$$

The biggest problem for the Bayesian MCI is the sparsity in the measurement space for a retrieval database with a finite number of cases. If we increase the length of the observation vector or decrease the measurement uncertainties, the number of database cases that match the observation vector become smaller and the Bayesian MCI fails. When this happens, the optimization process is begun to maximize the posterior PDF.

3.1 Radar-only retrievals

The optimization algorithm for radar retrievals is based on the robust and efficient OEM algorithm. OEM assumes that the forward model is moderately nonlinear and that both prior PDF and conditional PDF are Gaussians. OEM maximizes the posterior PDF by minimizing the following cost function:

$$J = (F(x) - y)^T S_y^{-1} (F(x) - y) + (x - x_a)^T S_a^{-1} (x - x_a) \quad (3)$$

where $F(x)$ is the forward model simulation, S_y and S_a are the covariance matrix for the measurement and prior uncertainties. In this study, the Levenberg-Marquardt minimization method (Rodgers, 2000) is implemented, and the required Jacobian matrix is calculated by perturbing the cloud microphysical parameters in each pixel. The initial state vector is constructed by implementing Bayesian MCI to each reflectivity value in different layers using the precalculated radar retrieval database described in Section 4.1. The posterior error covariance matrix specified below is used to characterize the retrieval uncertainties:

$$S = (S_a^{-1} + K^T S_y^{-1} K)^{-1} \quad (4)$$

where K is the Jacobian matrix to linearize the forward model. This covariance matrix is also derived based on the local Gaussian approximation and the forward model linearization assumption. The relative change of the cost function J is considered as the criteria for testing converge. The OEM optimization terminates if the relative change of J is below a specified threshold or the algorithm is over a certain number of iterations.

3.2 Radiometer-involved retrievals

The radiometer-involved retrievals that include the passive-only and the synergistic retrievals that also include radar do not use the OEM algorithm since it does not converge if the Jacobian matrix for BT is computed by perturbing vertically resolved ice cloud microphysical parameters. The applicable Jacobian matrix is usually obtained in two different ways. The first one is based on the adjoint modeling of radiative transfer. The adjoint approach is applied in some models like SHDOMPPDA (Evans, 2007), but it is not available in the ARTS forward model used here. A second approach is developed by the ARTS community, which does not calculate the BT sensitivity to the ice cloud microphysical parameters but to the scaling parameters in a normalized particle size distribution formalism proposed by Delanoe et al. (2005). In this study, however, since the in situ data are analyzed based on different PSD scheme and the a priori information is specified in terms of microphysical parameters, this approach is also not employed. Instead, we employ the ensemble approaches to handle the radiometer-involved optimizations. The ensemble approaches are discussed in the following two subsections.

3.2.1 synergistic retrievals

The synergistic radar and radiometer retrievals are done by extending the radar OEM algorithm to add the radiometer observations. The radar OEM algorithm provides the retrieved values and the associated uncertainty estimations. Following this step, the Cholesky decomposition is implemented on the covariance matrix and an ensemble of random cases with a correlated Gaussian distribution around the radar retrieved vector is generated. This is done by decomposing the covariance matrix into a lower triangular form and then multiplying the result by the standard normalized vectors. The corresponding BT simulations are subsequently computed by the radiative transfer model. The final retrieval results are calculated by the Bayesian MCI after evaluating the simulated cases according to their distance to the BT measurement vector, as indicated in Eq. (2).

3.2.2 radiometer-only retrievals

We employ the Ensemble Estimation Algorithm (EnEA) as the optimization procedure for radiometer-only retrievals. The EnEA was first proposed by Liu et al. (2018), and we continue to develop it as an optimization methodology. This algorithm is nominally proposed for the submillimeter-wave radiometer, but it is generally applicable to other remote sensors as well. The EnEA algorithm has advantages in the following aspects. First, the algorithm does not rely on gradient information to move forward. Since the Jacobian calculations are either complex to implement or computationally expensive, the EnEAs characteristic of no Jacobian dependence makes it suitable for ice cloud profile retrievals that have high dimensional state vectors using advanced radiative transfer models. Second, the EnEA is always is under the Bayesian MCI framework. This framework not only provides a solid theoretical basis but also offers a straightforward way to estimate the retrieval uncertainty associated with each retrieved quantity.

The EnEA stochastically explores the state vector space by sampling an explicit probability distribution function estimated from promising weighted cases found so far from the perspective of Bayesian MCI. The algorithm consists of two modules: the estimation module numerically estimates the unknown continuous posterior PDF using the discrete cases with posterior values in the last ensemble, and the sampling module synthesizes new cases according to the accumulated PDF. Started from the situation where too few a priori database cases matching the observations, the EnEA artificially inflates the measurement uncertainties so that there are enough matches between the observation vector and the BT simulations from the a priori profiles. The algorithm then computes the posterior values and applies a reselect procedure to make the weights of selected cases equivalent again. The covariance matrix of selected atmosphere profiles is calculated, and then it is used in a principal components method to generate new MCI cases having a Gaussian distribution around each of the selected cases, with the Gaussian deviates scaling with the previous posterior PDF. Once a new ensemble of random cases is synthesized and the corresponding BT is simulated, the algorithm evaluates these cases based on the prior PDF and likelihood PDF, and the optimization cycle starts again. As the iteration proceeds, the ensemble evolves and gradually becomes concentrated in the most likely area, compensating for the sparse distribution of the original retrieval database. The iteration stops when meeting a specified criterion, and the remaining cases in the last ensemble are used to calculate the mean parameter values (retrieved values) and standard deviations (retrieved uncertainties) by Bayesian MCI. More details about the algorithm implementation can be found in (Liu et al., 2018).

Several components in the EnEA method are updated in this study to make this algorithm more applicable in actual retrievals. Firstly, instead of only relying on the Global Environmental Multiscale Model (Cote & Staniforth, 1998) output, we build up a precalculated retrieval database according to the a priori PDF derived from in situ mea-

surements and space-borne radar measurements to make the synthesized ice cloud profiles more realistic and representative (Liu & Mace, 2020). Secondly, the retrieval performance of the EnEA is now evaluated by keeping the ice cloud vertical profiles in the a priori database and the ones used for testing to be completely independent. Thirdly, a new strategy is applied to deal with the regularization term that constrains the synthesized profiles to follow our prior knowledge. Liu et al. (2018) employed a normally distributed prior PDF which uses the Bayesian MCI estimates that are computed from the initial retrieval database by inflating measurement noise as the mean vector. The drawbacks of the method are twofold. First, the a priori PDF is required to be Gaussian, which made the EnEA less attractive since the algorithm is intended to handle the retrievals where prior PDF could have any functional form. Second, this method depends on a parameter to characterize the strength of the regularization. This parameter needs to be tuned experimentally, and the tuning itself could be a difficult optimization problem. In this study, the control vector transformation method applied in Evans et al. (2012) is employed. This allows the implementation of prior constraints even when the real a priori distribution is highly non-Gaussian. This method will be discussed in detail in Section 4.2.

4 Prior information

The key element in implementing the Bayesian MCI is to build up the retrieval database, which generally consists of two steps: creating random atmosphere and ice cloud properties that are distributed according to the prior PDF and computing the simulated radar reflectivity or BT using the forward model. In this study, we separately develop two prior databases for radar and radiometer retrievals using prior information from in situ measurements and CloudSat observations.

4.1 Radar retrieval database

The realistic ice cloud microphysical probability distributions used for building up the radar retrieval database is obtained from the in situ data from instruments flown in the TC4 campaign. The in situ ice particle size distribution (PSD) is obtained from the two-dimensional stereo (2D-S) probe and the precipitation imaging probe (PIP). The bimodal PSD scheme which approximates both small and large particle distribution modes by gamma functions is used to fit the in situ data, and the ice cloud parameters, including ice water content (IWC), number concentration (NC), and particle size are derived. More details about TC4 in situ analysis could be found in (Liu & Mace, 2020). A multivariant Gaussian distribution in temperature, $ln(IWC)$, and $ln(NC)$ is used to capture the in situ statistics, using the prior idea that the microphysical parameters are approximately lognormally distributed. Using a multi-variant Gaussian function shows several advantages in generalizing the in situ statistics: first, it specifies the microphysical PDF using a few parameters; second, it facilitates the following radar OEM algorithm, which explicitly requires a normally distributed prior PDF; third, it reasonably covers the space where the in situ probes fail to detect, which is important since the random cases need to completely cover the possible parameter range. The parameters for the TC4 multivariant Gaussian function are summarized in Table 1. A number of random cases (30,000 cases in this study) are sampled from the Gaussian function, and the ARTS radar forward model is used to simulate the reflectivity for each random case.

Figure 5 shows the two-dimensional histogram for the microphysical quantities and reflectivity simulations in the radar retrieval database. The middle panel and the right panel indicate that the radar reflectivity simulations have a strong correlation with IWC in the whole range, but its correlation with NC is much weaker.

Table 1. Ice particle microphysical statistics defining the a priori Gaussian probability distribution derived from the TC4 in situ data

	ln(IWC) (g/m^3)	ln(NC) (/m^3)	Temperature (K)
mean	-6.04	9.88	231.07
std	2.45	1.81	12.41
correlation	$\rho_{ln(iwc)-ln(nc)} = 0.69$	$\rho_{ln(iwc)-tp} = 0.17$	$\rho_{ln(nc)-tp} = -0.10$

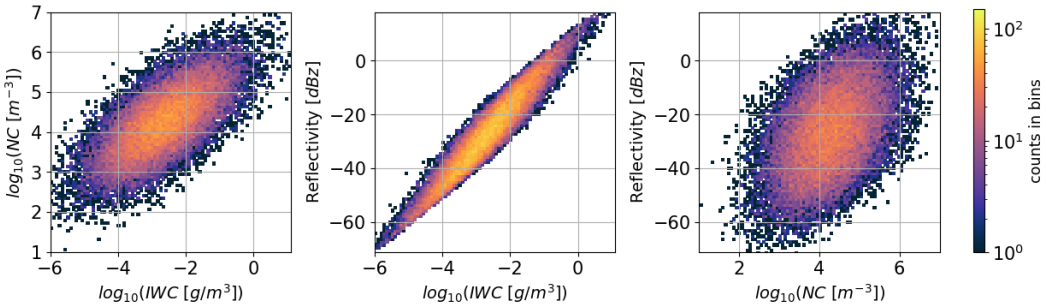

Figure 5. Two-dimensional histogram for the microphysical quantities and the W-band radar reflectivity simulations derived from the random cases in the precalculated radar retrieval database.

4.2 Radiometer retrieval database

Apart from using the TC4 in situ microphysical statistics, we also use the CloudSat observations to acquire the critical coherent vertical correlations to synthesize the random ice cloud profiles for radiometer retrieval database creation. The data we use include CloudSat radar reflectivity, CALIPSO lidar cloud fraction, and the corresponding ECMWF profiles of temperature and relative humidity. The active remote sensing data profiles are combined with the TC4 cloud microphysical probability distributions where we employ the Bayesian MCI algorithm to create vertical profiles of microphysical properties that are consistent with the measurements and the in situ statistics. After that, the cumulative distribution functions (CDFs) and empirical orthogonal functions (EOFs) procedures are applied to capture the complete single-point and two-point statistics and then to create any number of synthetic microphysical and thermodynamic profiles (100,000 profiles in this study) that are statistically consistent with the Bayesian retrieval results. A comprehensive discussion on creating synthetic ice cloud profiles can also be found in Liu and Mace (2020).

As mentioned in section 3.2.2, we employ the control vector transformation method to implement the prior constraint. The CDFs are used to capture the one-point statistics by sorting the variable at different layers from smallest to largest in value and calculating the sum of the assigned equal probabilities up to each datum. The percentile ranks at different layers are transformed into Gaussian derivate matrix using the standard normal cumulative distribution function:

$$\xi_i = \phi^{-1}(R(x_i)) \tag{5}$$

where $\phi(\xi)$ is the standard normal cumulative distribution function, and $R(x_i)$ is the percentile ranks for different parameters at different layers. For a new ensemble, the strength of the prior constraints for different ice cloud profiles is determined by their ξ values. This step allows the implementation of a more realistic prior PDF that is captured by the CDFs.

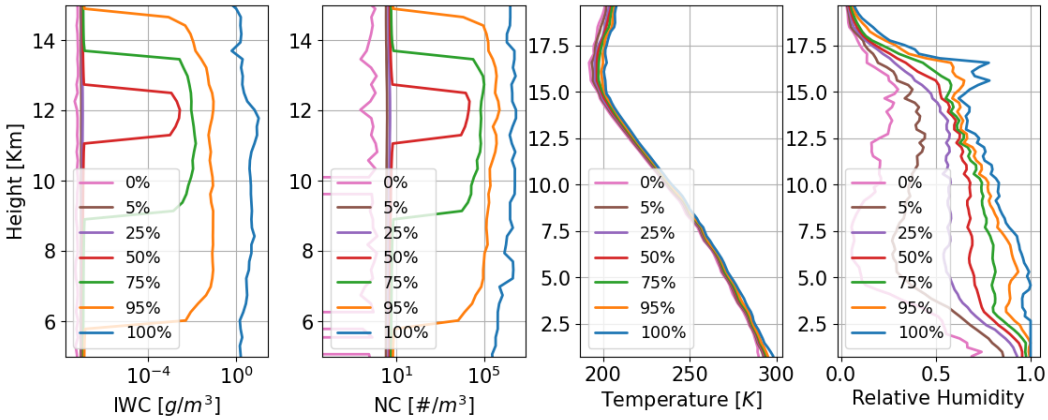

Figure 6. Profiles of ice water content (IWC), number concentration (NC), temperature, and relative humidity for seven percentiles in the cumulative distributions for the random atmospheric/cloud profiles in the precalculated radiometer retrieval database.

Figure 6 shows the profiles of IWC, NC, temperature, and relative humidity for seven percentiles in the cumulative distributions. Layers that are identified as clear are added with random Gaussian noise to prevent discontinuity in the CDFs. The mean values for the added IWC and NC noise are 10^{-6}g/m^3 and 10 m^{-3}, respectively. The left two panels show that the a priori IWC profiles cover the range from clear condition to about 10 g/m^3, and the NC profiles cover the range up to about 10^6m^{-3}. The 50% curve only has meaningful values in the 11 to 13 km high range, indicating that the ice cloud particles are mostly concentrated in this region. The 75% curve implying that a large majority of atmospheric conditions outside the 9 to 14km range are effectively clear. The right two panels show that the a priori temperature profiles have a small range of temperature coverage under the tropical atmospheric conditions applied in this study, and the relative humidity profiles have a large possible range, almost coving the entire possible values from 0 to 1.

The precalculated retrieval database provides a good opportunity for estimating the degrees of freedoms (DoF) for the ACCP radiometer. The DoF describes the number of independent pieces of information in the radiometer measurement since some channels provide redundant information. The DoF is usually calculated as the trace of the averaging kernel matrix based on the Jacobian matrix (Rodgers, 2000), but a more general method described in Eriksson et al. (2020) is employed here since the Jacobian matrix for BT is not available in this study. This method calculates the DoF in the measurement space based on the Empirical Orthogonal Function (EOF) approach. The covariance matrix of a set of simulated BT is decomposed using EOF:

$$S_y = E\Lambda E^T \tag{6}$$

where E is the eigenvector and Λ is the diagonal matrix containing the corresponding eigenvalues. The Gaussian measurement noise in eigenspace is transformed back using the same eigen coordinate axes:

$$S_\Lambda = ES_\xi E^T \tag{7}$$

where S_ξ is the diagonal matrix that contains the square of measurement noise for different channels. The DoF is defined as the number of diagonal elements in S_y that are larger than the corresponding value in S_Λ in the same place.

Figure 7 shows the DoF of the ACCP radiometer as the function of the ice water path (IWP) and integrated water vapor (IWV). The necessary radiometer measurement

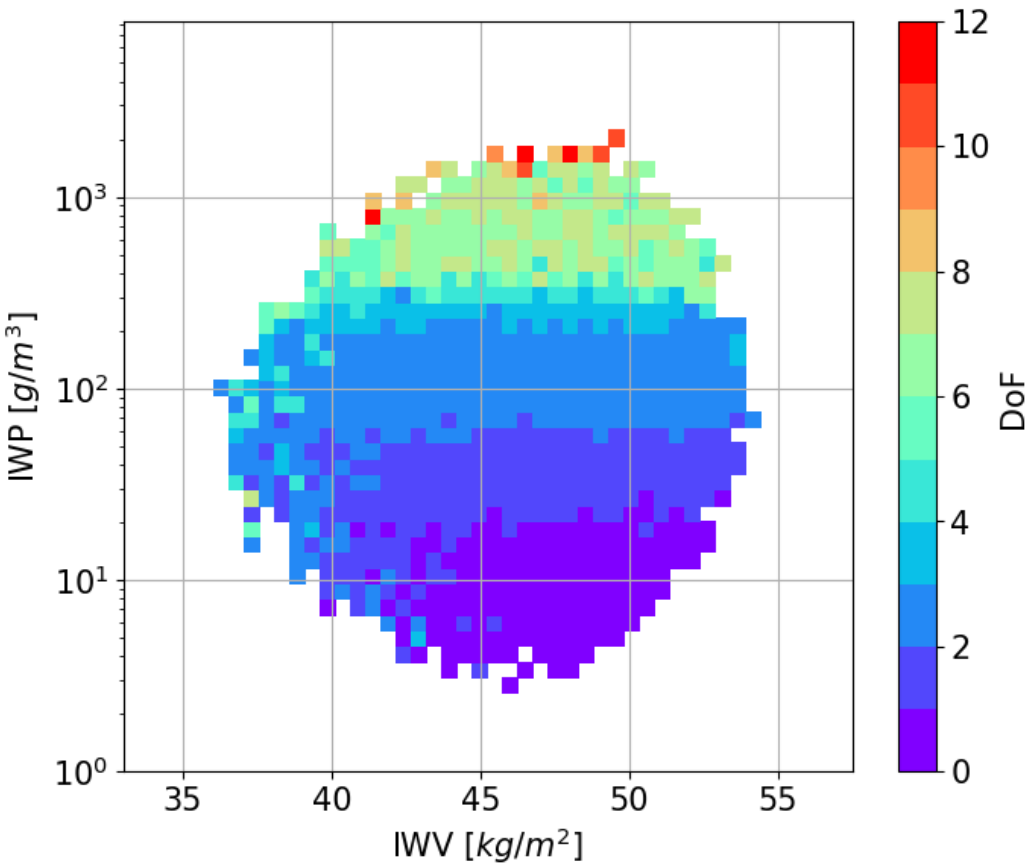

Figure 7. The Degree of Freedoms (DoF) for the ACCP radiometer as the function of the ice water path and integrated water vapor. The DoF is estimated using the radiometer retrieval database that has 100,000 random atmospheric/cloud profiles.

noise is configured by referring to the CoSSIR uncertainties that are obtained from calibration target fluctuation statistics applied in Evans et al. (2012). The double-sideband channels for 118 GHz, 183 GHz, 380 GHz are set to have uncertainties of 1.5K, 1.6K, 2.3K, and the window channels uncertainties for 240 GHz, 310 GHz, 660 GHz, 880 GHz are set to be 2.0 K, 2.3 K, 2.5 K, 4.0K, respectively. The DoF is computed only when the number of random cases in a certain IWV-IWP range is larger than 10 to avoid noise interference. It can be seen that the DoFs increase with IWP. The DoFs are mostly zero when the IWP values are smaller than 20 g/m^2, indicating the ACCP radiometers limitation for IWP detection. The DoFs generally equal to 1 in 20 to 70 IWP range, and equal to 2 in 70 to 110 IWP range. This analysis is consistent with the plots in Figure 4, which show that only the 660Ghz and 880 GHz channels are sensitive to the thin cirrus clouds. When IWP is over 300 g/m^2, the DoF is mostly between 6 to 8, and the DoF is over 10 very occasionally.

5 Retrieval Simulation Experiment and Results

We conduct simulated retrieval experiments to evaluate the retrieval accuracy of ice cloud microphysics for the objective ACCP remote sensors. The simulation observations for the W-band radar and the submillimeter-wave radiometer under the selected reference cloud scenes are presented in section 3.1. After adding measurement noise, the

simulated observations are input to the hybrid Bayesian algorithms to retrieve desired quantities and uncertainty estimates. The retrieved parameters are then compared to the true values to quantitively assess the retrieval accuracies.

Several configurations in the hybrid Bayesian algorithms are summarized here. The independent Gaussian noise with standard deviation according to the absolute instrument accuracy (1 dBz in this study) is added to the simulated radar observations, but we applied 4 dBz Gaussian noise in the Bayesian retrievals to also include the forward model uncertainty that would be realized from imperfect knowledge of ice crystal bulk density to make the simulation experiments more realistic. The 4 dBz measurement uncertainty is estimated based on the study of Mace and Benson, 2017. Similarly, the Gaussian noise of 1K is added to the simulated BT in each channel to characterize the absolute accuracy, but more realistic uncertainty estimations specified in section 4.2 are used in the Bayesian retrievals. For the radar-only retrievals, the initial state vector for the OEM optimization is stochastically generated layer by layer based on the Bayesian MCI algorithm using the precalculated radar retrieval database. The retrieval process precedes from top down, and the generated radar attenuation is used to correct the radar reflectivity below. The Bayesian MCI retrievals are only applied to the layers with corrected radar reflectivity larger than the minimum sensitivity (-30 dBz). The a priori PDF used in the OEM optimization only utilizes the statistical Gaussian parameters listed in Table 1, and the vertical correlations between ice cloud microphysics at different layers are not considered. For the synergistic retrievals, 500 random cases are generated from the radar OEM retrieval results to add BT measurement information using Bayesian MCI. For the radiometer-only retrievals, the ensemble estimation retrievals stop when either of the two following termination criteria is satisfied: a number of random cases (25 cases in this study) matching the observations within a specified χ^2 threshold are obtained in one ensemble, or the number of iterations exceeds a specified value. The χ^2 threshold is set as $M+4\sqrt{M}$, where M is the number of radiometer channels. This configuration is based on the fact that the mean value and variance of the χ^2 istribution are M and 2M, respectively. Considering that the radiative transfer simulations for an ensemble of atmospheric and cloud profiles are computationally intensive, the limitation for the number of iterations is set to be 3. 500 random cases in the first ensemble and 100 cases in the following two ensembles are generated to statistically explore the state vector space.

Figure 8 and figure 9 show the direct comparison between the true values and the retrieval results for IWC and NC profiles along the ECCC model transect. The retrieval results for radar-only, radiometer-only, and combined are presented sequentially. We find that there is essentially no information regarding the ice cloud vertical profiles in the radiometer measurements. For the active-only retrievals, the retrieved IWC profiles realistically reproduce the vertical structure of the reference cloud scenes. The retrieve values also correspond to the true values in general, even though sometimes the retrievals tend to underestimate the IWC values, especially on the top of the cloud ranging from 10 km to 15 km in height. By contrast, the active-only retrievals for NC profiles perform much worse. The true NC values cover the range from 10 m^{-3} to over 10^6 m^{-3}, but the radar retrievals do not vary too much, usually concentrating around domains in 10^3 m^{-3} to 10^5 m^{-3} range. The retrieval results again illustrate that the radar measurements are much more sensitive to the IWC variation of IWC compared to the NC variation. For the synergistic retrievals, obvious perturbations can be observed for both IWC and NC profiles and the results become less smooth compared to the radar-only retrievals. The added radiometer observations tend to correct the IWC underestimation discussed above.

Before we further analyze the retrieval results quantitively, we would like to investigate the effectiveness of the updated ensemble estimation algorithm first. The algorithm is now evaluated by ensuring the independence between the vertical profiles in the precalculated prior database and the ones in the reference cloud scenes. Also, a new strategy regarding the addition of prior constraints during ensemble optimization is imple-

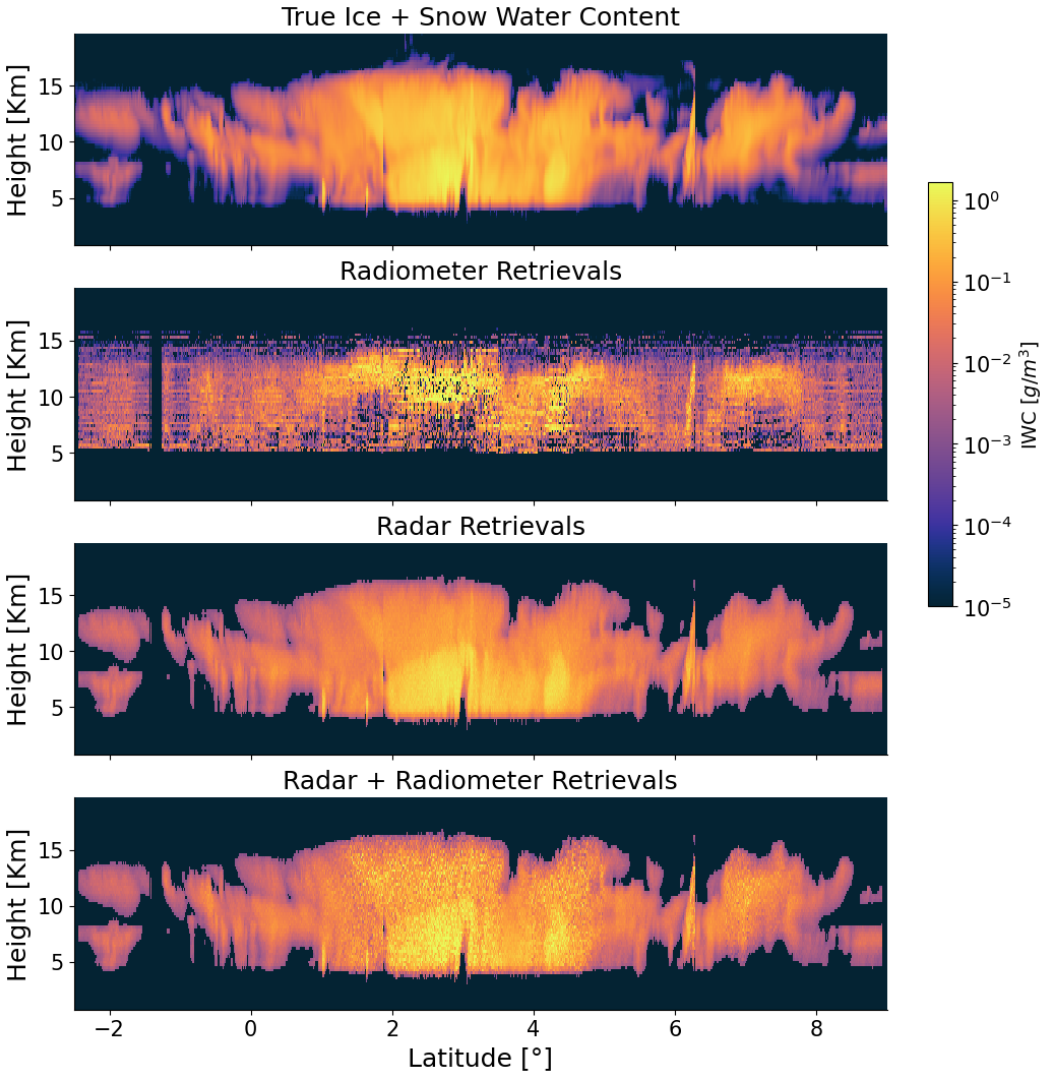

Figure 8. Comparison between the true values and the retrieval results for ice water content profiles along the selected latitude transect. The retrieval results for radar-only, radiometer-only, and combined are presented sequentially.

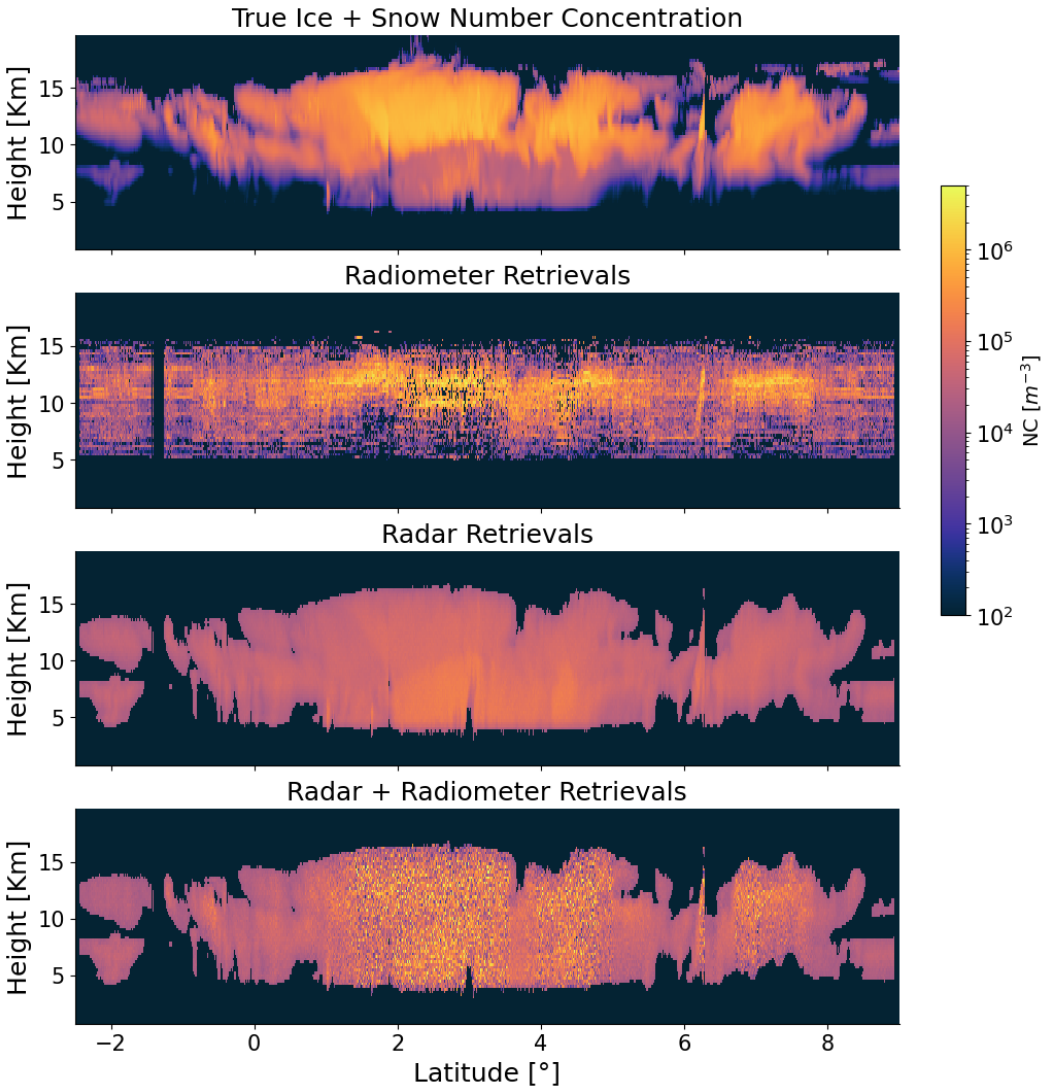

Figure 9. Same as figure 8 but for the retrieval results of number concentration.

mented. The top panel of figure 10 shows the comparison of the minimum χ^2 values that exist in the a priori database and in the last ensemble after optimization. The χ^2 threshold determined by the number of channels is also shown in a dotted grey line. The decrease of the cost function is observed over the whole range, indicating that the BT simulations after optimization better reproduce the measurements within the observation uncertainties. For most of the input BT measurements, the best database cases have χ^2 values smaller than 100, implying that the prior radiometer database with 100,000 random cases covers the BT space well. In these situations, the ensemble estimation algorithm generally reduces the cost function below the specified χ^2 threshold. In the region between 2 to 4 latitude, the minimum χ^2 values in the a priori database are always over 100, indicating the inevitable sparsity in the measurement space for a database with a finite number of discrete samples. The corresponding optimized χ^2 values are still large, but the χ^2 reduction compared to the original values is clear. The bottom panel shows the comparison of the retrieved IWP before and after the ensemble estimation optimization. The retrievals before ensemble optimizations are computed by Bayesian MCI using the a priori database, even though only a few cases have contributions to the integration. The true IWP values are shown in a black dot line for reference. We find that the database retrievals closely follow the true IWP values under the thin ice cloud situation, but we find a clear underestimation when the IWP is over 10^3 g/m^2. The database retrieval accuracies are highly correlated to the χ^2 value shown on the top panel. Some database retrievals remain the same for different BT input between 2 to 4 latitude, implying the fact that the same database cases respond to different observations during MCI, which further indicates the sparse distributions in the relevant BT space region. The optimization retrievals do not make clear differences when the IWP values are small, but noticeable improvements are seen when IWP is over a certain value. These figures demonstrate that the ensemble estimation algorithm effectively improves the retrieval performance compared to the retrievals that only depend on the a priori database. Only the ensemble estimation retrieval results are discussed below.

Figure 11 shows the retrieved IWP values for the passive-only, radar-only, and combined retrievals based on the hybrid Bayesian algorithms. The top panel directly compares the retrieved IWP to the true values along the latitudinal transect, and the bottom panel shows the logarithmic errors to make the comparisons clearer. The logarithmic error is defined as:

$$E_{log10} = log_{10}(\frac{x_{retrieved}}{x_{true}}) \tag{8}$$

and the 0 dB logarithmic error represents that the retrieved value and true value are identical. For the passive-only retrievals, the retrieval errors when IWP is smaller than 100 g/m^2 are high, but the errors become comparable to the active-involved retrievals in other circumstances. The active-only retrievals show the tendency to overestimate the IWP for thin clouds but underestimate the thick cloud IWP. The combined retrievals are developed from the radar OEM results, and substantial improvements in IWP retrieval accuracy can be seen after adding the ACCP BT measurements. Most retrieval errors are between -0.5 dB and 0.5 dB.

Figure 12 shows the mean IWP absolute logarithmic error in each IWP increment as a function of IWP. As expected, the radiometer-only retrieval errors are large for the low IWP because the corresponding DoF is very low. The retrieval errors increase when IWP is over 10^3 g/m^2, which is primarily because the a priori database does not densely cover the relevant region. The IWP absolute errors for the radar-only retrievals remain low for the thin cloud. The errors increase when IWP is over 300 g/m^2, generally higher than the passive-only retrievals under the same cloud scenes. The combined retrievals have significant improvements over the whole range, and the mean errors are mainly around 0.1 dB.

Figure 13 shows the scatterplots of the retrieved parameters against the true values that are colored by density to visualize the retrieval performance. The scatterplots

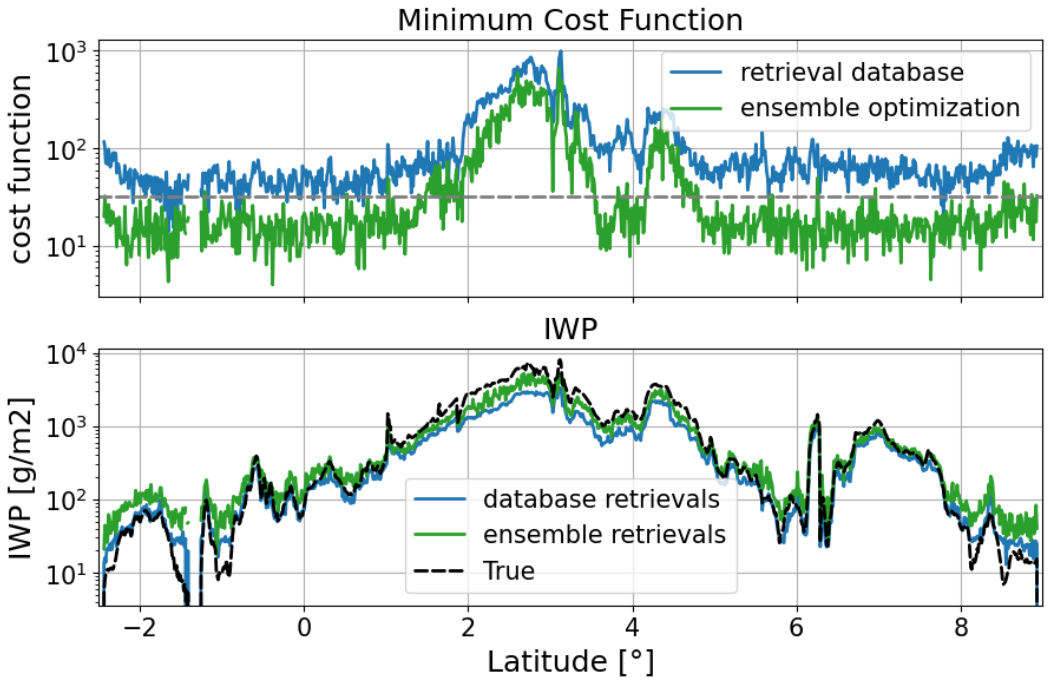

Figure 10. The top panel shows the comparison of the minimum 2 values that exist in the a priori database and in the last ensemble after optimization for the given brightness temperature observations. The bottom panel shows the comparison of the retrieved ice water path (IWP) before and after the ensemble estimation optimization.

for IWC, NC, and IWP are shown in different columns, and the plots for passive-only, active-only, and combined retrievals are shown in different rows. Starting from the IWC retrievals in the first column, the passive-only retrievals show the largest deviations from the diagonal line, which is not surprising since the BT measurements have low sensitivity to the vertical distribution of the ice cloud microphysics. The radar-only retrievals provide much more accurate results. The scatter of points lies along the diagonal and the associated deviations are small. The radar-only retrievals are observed to bias high for the tenuous cases and bias low when IWC values are high. The reason for the low-end biases is that the radar reflectivity drops below the specified radar sensitivity, and the biases at the high end are due to non-Rayleigh effects and attenuation. The combined retrievals correct the high-end offset, and the scatter plots lie more along the diagonal. The deviations of the combined retrievals are observed to become large. This is because the BT measurements are added through an ensemble approach, which generates random cases over a large possible range to statistically explore the state vector space. For the NC retrievals in the second column, the passive-only retrievals again show very little skill. The NC results from the radar-only retrievals do not follow the true values well. The retrieved values are always located in the range of $10^4\ m^{-3}$ to $10^5\ m^{-3}$, although the true values vary in a much wider range. The combined retrievals improve the NC accuracies a little, but the overall performance is still poor. The IWP retrievals show very good performance overall. All retrieved values in different panels follow the true values with small associated deviations. The IWP results from passive-only tend to underestimate the true values when IWP is small and overestimate the true values when IWP is large. The overestimation performance could possibly be corrected if more random atmospheric/cloud profiles covering the large IWP range are included in the pre-calculated radiometer retrieval database. The active-only retrievals show a similar ten-

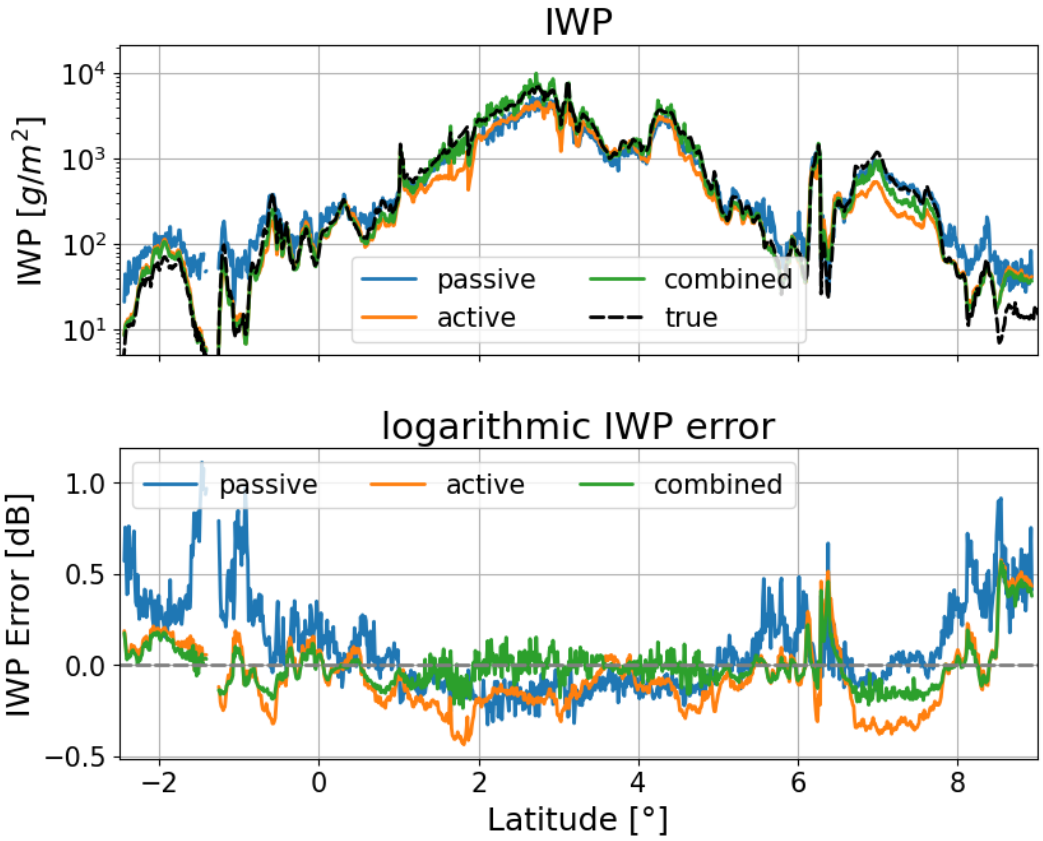

Figure 11. The top panel shows direct comparison between the retrieved ice water path (IWP) and the true values along the latitudinal transect. The passive-only, radar-only, and combined retrievals are all displayed. The bottom panel shows the logarithmic errors for different retrievals to make the comparisons clearer.

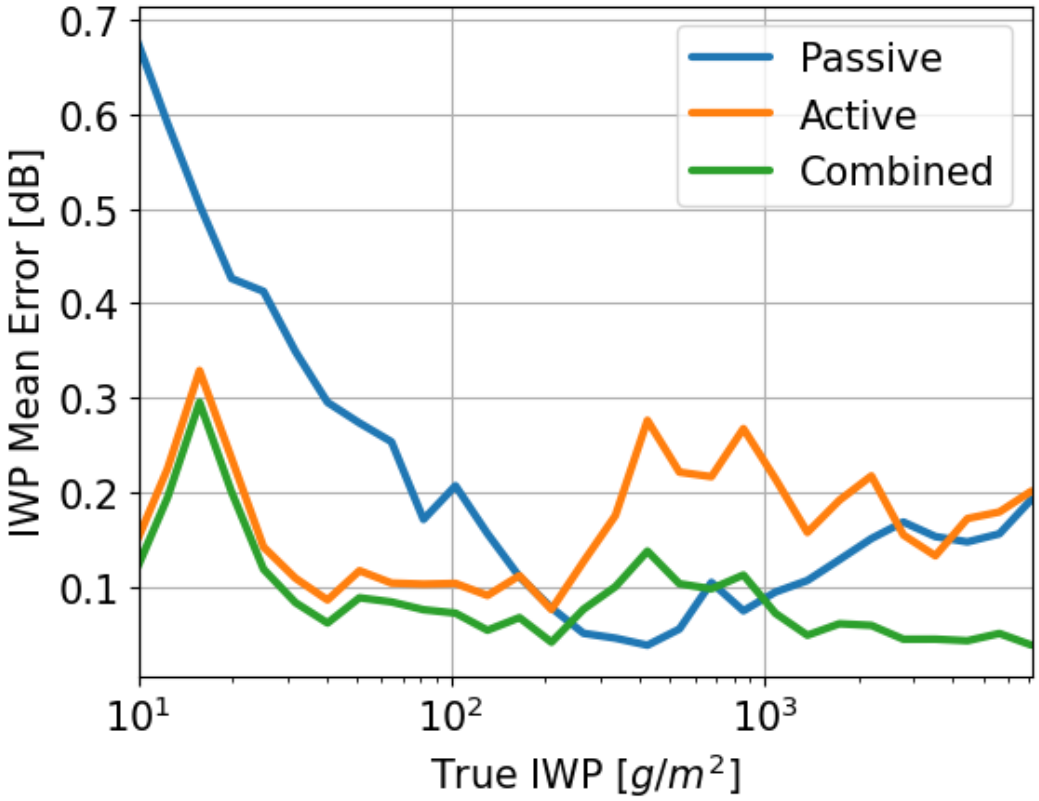

Figure 12. The mean ice water path (IWP) absolute logarithmic error in each IWP increment as a function of IWP for different retrievals.

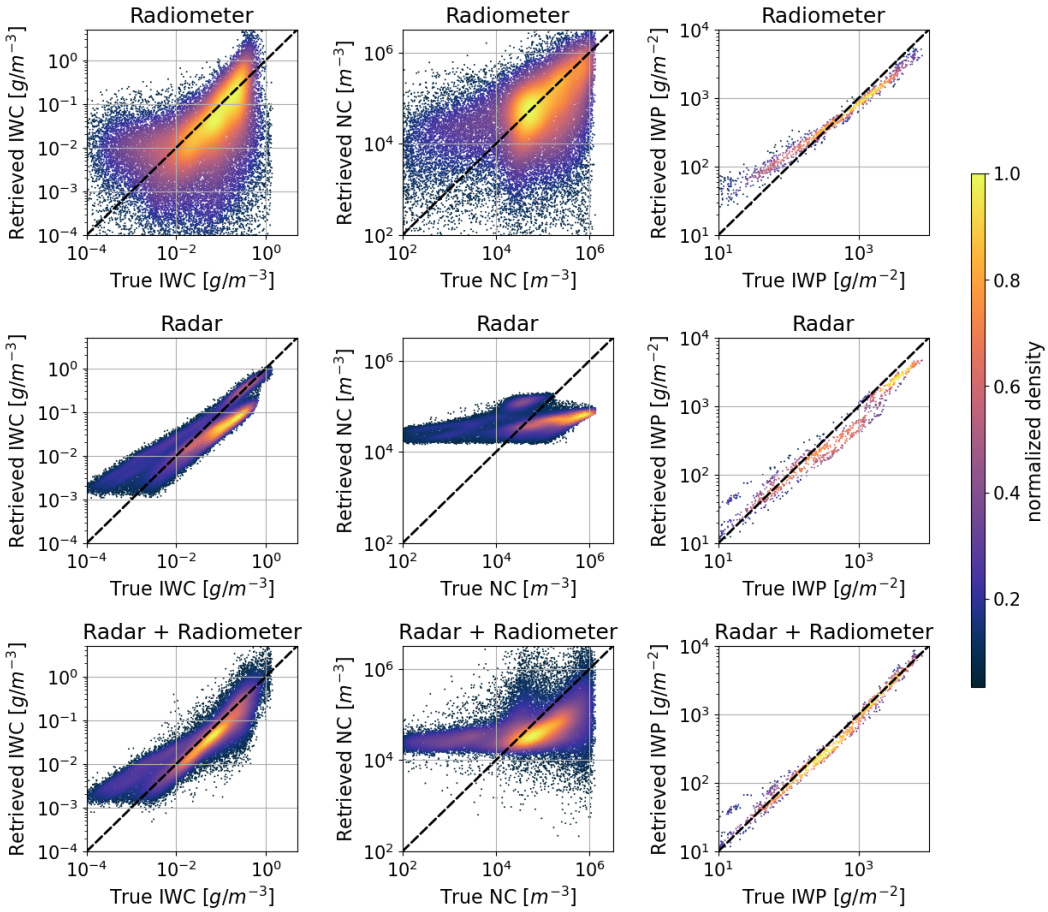

Figure 13. The scatterplots of the retrieved parameters against the true values that are colored by density. The scatterplots for ice water content (IWC), number concentration (NC), and ice water path (IWP) are shown in different columns, and the plots for passive-only, active-only, and combined retrievals are shown in different rows.

dency, and significant improvements could be seen for the results from the combined retrievals.

Figure 14 displays the PDF of the logarithmic errors for different parameters under different retrieval methods to more quantitively assess the retrieval performance. As displayed in the left panel, the IWC logarithmic errors for radiometer-only retrievals cover a large range from -4 dB to 2 dB, and the radar-only and combined retrievals are mostly concentrated between -1 dB to 1 dB. Compared to the error PDF for radar-only retrievals, the PDF for the synergistic retrievals has a smaller offset and smaller variance, even though the improvements are not substantial. The NC retrievals displayed in the middle panel show little skill with the logarithmic error spreading from -2.5 dB to 2.5 dB. As for the IWP retrieval displayed in the right panel, the passive-only and active-only retrievals show comparable errors, both distributing between -0.5 dB to 0.5 dB, and significant improvements for the synergistic retrievals is evident. Figure 15 shows the quantitative statistics of the absolute logarithmic error to summarize the PDF information. The left panel shows the commonly used root-mean-square deviation (RMSD) for different parameters. Since the RMSD is easily skewed by a few poor retrievals, the median errors that sep-

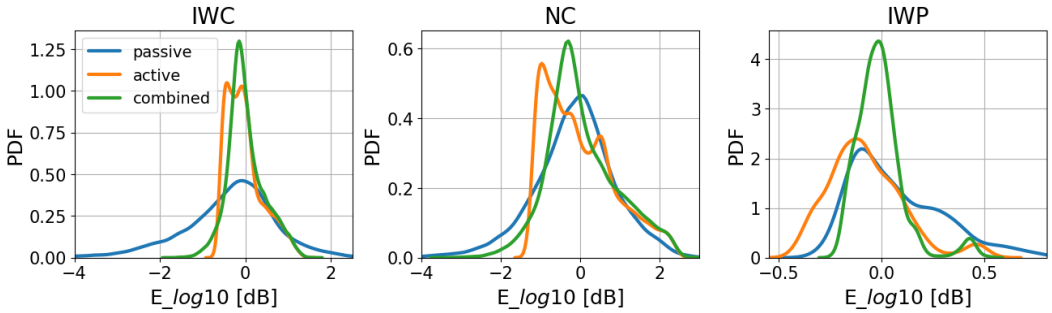

Figure 14. The probability density function (PDF) of the logarithmic errors for different ice cloud parameters under different retrieval methods.

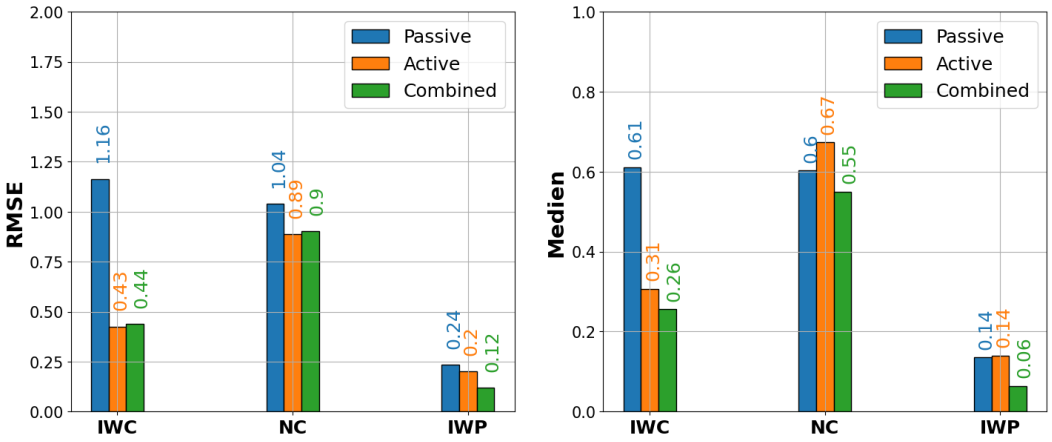

Figure 15. The quantitative statistics of the absolute logarithmic error for the retrieved ice cloud quantities. The left panel shows the root-mean-square deviation (RMSD), and the right panels show the median errors that separate the higher half from the lower half in all the retrieval error estimations.

arate the higher half from the lower half in all the retrieval error estimations are displayed in the right panel.

6 Summaries

In this study we develop a suite of hybrid Bayesian retrieval algorithms for millimeter-wave radar and submillimeter-wave radiometer to assess the ACCP observing system capability in sensing ice cloud microphysical quantities. The geophysical variables we investigate include the IWC, NC, and IWP. The hybrid Bayesian algorithms combine the Bayesian MCI and optimization processes to compute retrieval quantities and associated uncertainties. The radar-only retrievals employ the OEM optimization algorithm that uses gradient information to minimize the cost function. The OEM is initialized by a state vector that is constructed by implementing Bayesian MCI to each reflectivity value in different layers using the precalculated radar database. The necessary Jacobian matrix is calculated by perturbing the ice cloud microphysical quantities in different layers. The radiometer-involved retrievals employ ensemble strategies to optimize the ill-posted problem. The synergistic radar and radiometer retrievals are done by generating random cases from the radar OEM results based on the Cholesky decomposition technique. The BT

simulations are then computed, and the Bayesian MCI is implemented to derive the final retrieval results. For the radiometer-only retrievals, the ensemble estimation algorithm is applied to statistically estimate the posterior pdf using the promising weighted cases. The estimation module and the sampling module proceed iteratively to stochastically explore the state vector space. In addition, a new approach to implement prior constrain that allow the a priori PDF to be highly non-Gaussian is proposed to make the ensemble algorithm more applicable.

We conducted simulation experiments to evaluate the accuracy of retrieving ice cloud quantities for different remote sensors. The simulated noisy observations are input to the hybrid Bayesian algorithms, and the retrieved parameters are compared to the known values to determine the retrieval accuracies. A tropical transect of cloud profiles that are simulated using the ECCC model is selected as the reference cloud scenes. This choice ensures the independence between the atmospheric/cloud profiles for testing and the vertical profiles in the a priori database. The retrieval of NC remains poor across the various methods. We speculate that the addition of an observational constraint such as lidar or visible reflectance will be needed to address NC. This will be the topic of future work. Also, we find that the radiometer observations provide little vertical information on IWC. The radar-only retrievals demonstrate skill in retrieving the IWC although the radar-only IWC retrieval biases high for tenuous volumes where the radar reflectivity drops below the sensitivity of the radar. At the high end, the radar-only IWC retrieval biases low due to non Rayleigh effects and attenuation. In future work, we will explore the skill added by lidar at the low end and lower frequency radar channels at the high end. The synergistic radar and radiometer retrievals provide significant improvements in IWP.

This paper provides an end-to-end idealized simulation experiment that sacrifices precise reality in order to demonstrate nuances in the various algorithms. Several disadvantages are worth mentioning. Firstly, the reference cloud scenes only contain frozen hydrometers, and the retrieval performance under more complex atmospheric scenarios is not investigated. Also, the forward model in this study only applies the EvansSnow particle habit, and the uncertainties caused by various particle habits are not considered. Secondly, the statistical characteristics are only derived based on selected atmospheric/cloud profiles along a latitudinal transect. Since this subset with a finite number of profiles can hardly represent the realistic spatial distribution of ice cloud microphysics, the statistics we derive may differ from the characteristics of the entire possible atmospheric conditions. Thirdly, apart from the W-band radar and the submillimeter-wave radiometer, the ACCP observing system includes other remote sensors that would be highly helpful to improve retrieval accuracies for ice cloud remote sensing. For instance, highly accurate Doppler velocity measurements may allow for constraints on the ice crystal bulk density that could significantly mitigate forward model uncertainties. The retrieval performance by combining other synergistic information content remains to be investigated.

Acknowledgments

This research was supported by NASA Grants NNX15AK17G and 80NSSC19K1087 both administered from the Goddard Space Flight Center under the NASA ACE and ACCP programs, respectively. We thank for Prof. Pavlos Kollias at Stony Brook University for providing the atmospheric scenes from the ECCC model that we used for evaluating the synergistic retrievals. The TC4 in situ data for this study were collected by the members of the Stratton Park Engineering Corporation led by Paul Lawson, as well as Andrew Heymsfield at the National Center for Atmospheric Research. The CloudSat data were obtained from the CloudSat Data Processing Center at the Colorado State Universitys Cooperative Institute for Research in the Atmosphere (CIRA). All TC4 data are publicly and freely available in the NASA data archive at https://espoarchive.nasa.gov/archive/browse/tc4, and the CloudSat data are available at http://www.cloudsat.cira.colostate.edu/data-products.

References

Ackerman, T., Liou, K., Valero, F., & Pfister, L. (1988). Heating rates in tropical anvils. *Journal of the atmospheric sciences*, *45*(10), 1606–1623.

Berry, E., & Mace, G. (2014). Cloud properties and radiative effects of the asian summer monsoon derived from atrain data. *Journal of Geophysical Research: Atmospheres*, *119*(15), 9492–9508.

Board, S., National Academies of Sciences, E., & Medicine. (2019). Thriving on our changing planet: A decadal strategy for earth observation from space. *National Academies Press*.

Brath, M., Ekelund, R., Eriksson, P., Lemke, O., & Buehler, S. (2020). Microwave and submillimeter wave scattering of oriented ice particles. *Atmospheric Measurement Techniques*, *13*(5), 2309–2333.

Brath, M., Fox, S., Eriksson, P., Harlow, R., Burgdorf, M., & Buehler, S. (2018). Retrieval of an ice water path over the ocean from ismar and marss millimeter and submillimeter brightness temperatures. *Atmospheric Measurement Techniques*, *11*(1), 611–632.

Buehler, S., Defer, E., Evans, F., Eliasson, S., Mendrok, J., Eriksson, P., ... Kasai, Y. (2012). Observing ice clouds in the submillimeter spectral range: the cloudice mission proposal for esa's earth explorer 8. *Atmospheric Measurement Techniques*, *5*(7), 1529–1549.

Buehler, S., Eriksson, P., Kuhn, T., Von Engeln, A., & Verdes, C. (2005). Arts, the atmospheric radiative transfer simulator. *Journal of Quantitative Spectroscopy and Radiative Transfer*, *91*(1), 65–93.

Chen, J., Pendlebury, D., Gravel, S., Stroud, C., Ivanova, I., DeGranpr, J., & Plummer, D. (2018). Development and current status of the gem-mach-global modelling system at the environment and climate change canada. *In International Technical Meeting on Air Pollution Modelling and its Application*, 107-112.

Cote, G. S. M. A. P. A. R. M., J., & Staniforth, A. (1998). The operational cmcmrb global environmental multiscale (gem) model. part i: Design considerations and formulation. *Monthly Weather Review*, *126*(6), 1373-1395.

Delanoe, J., Protat, A., Testud, J., Bouniol, D., Heymsfield, A., Bansemer, A., ... Forbes, R. (2005). Statistical properties of the normalized ice particle size distribution. *Journal of Geophysical Research: Atmospheres*, *110*(D10).

Eriksson, P., Buehler, S., Davis, C., Emde, C., & Lemke, O. (2011). Arts, the atmospheric radiative transfer simulator, version 2. *Journal of Quantitative Spectroscopy and Radiative Transfer*, *12*(10), 1551–1558.

Eriksson, P., Ekelund, R., Mendrok, J., Brath, M., Lemke, O., & Buehler, S. (2018). A general database of hydrometeor single scattering properties at microwave and sub-millimetre wavelengths. *Earth System Science Data*, *10*(3), 1301–1326.

Eriksson, P., Rydberg, B., Mattioli, V., Thoss, A., Accadia, C., Klein, U., & Buehler, S. (2020). Towards an operational ice cloud imager (ici) retrieval product. *Atmospheric Measurement Techniques*, *13*(1), 53–71.

Evans, K. (2007). Shdomppda: A radiative transfer model for cloudy sky data assimilation. *Journal of the atmospheric sciences*, *66*(11), 3854–3864.

Evans, K., Walter, S., Heymsfield, A., & McFarquhar, G. (2002). Submillimeterwave cloud ice radiometer: Simulations of retrieval algorithm performance. *Journal of Geophysical Research: Atmospheres*, *107*(D3), AAC-2.

Evans, K., Wang, J., Racette, P., Heymsfield, G., & Li, L. (2005). Ice cloud retrievals and analysis with the compact scanning submillimeter imaging radiometer and the cloud radar system during crystal face. *Journal of Applied Meteorology*, *44*(6), 839–859.

Evans, K., Wang, J., Starr, O., Heymsfield, G., Li, L., Tian, L., ... Bansemer, A. (2012). Ice hydrometeor profile retrieval algorithm for high-frequency

microwave radiometers: application to the cossir instrument during tc4. *Atmospheric Measurement Techniques*, *5*(9), 2277–2306.

Hartmann, D., & Berry, S. (2017). The balanced radiative effect of tropical anvil clouds. *Journal of Geophysical Research: Atmospheres*, *122*(9), 5003–5020.

Jimenez, C., Buehler, S., Rydberg, B., Eriksson, P., & Evans, K. (2007). Performance simulations for a submillimetrewave satellite instrument to measure cloud ice. *Quarterly Journal of the Royal Meteorological Society: A journal of the atmospheric sciences, applied meteorology and physical oceanography*, *133*(s2), 129–149.

Kangas, V., D'Addio, S., Klein, U., Loiselet, M., Mason, G., Orlhac, J., ... Thomas, B. (2014). Performance simulations for a submillimetrewave satellite instrument to measure cloud ice. *Ice cloud imager instrument for MetOp Second Generation. In 2014 13th Specialist Meeting on Microwave Radiometry and Remote Sensing of the Environment (MicroRad)*, 228–231.

Liou, K. (1986). Influence of cirrus clouds on weather and climate processes: A global perspective. *Monthly Weather Review*, *114*(6), 1167–1199.

Liu, Y., Buehler, S., Brath, M., Liu, H., & Dong, X. (2018). Ensemble optimization retrieval algorithm of hydrometeor profiles for the ice cloud imager submillimeterwave radiometer. *Journal of Geophysical Research: Atmospheres*, *123*(9), 4594–4612.

Liu, Y., & Mace, G. (2020). Synthesizing the vertical structure of tropical cirrus by combining cloudsat radar reflectivity with in situ microphysical measurements using bayesian monte carlo integration. *Journal of Geophysical Research: Atmospheres*, *125*(18), e2019JD031882.

Pfreundschuh, S., Eriksson, P., Buehler, S., Brath, M., Duncan, D., Larsson, R., & Ekelund, R. (2020). Synergistic radar and radiometer retrievals of ice hydrometeors. *Atmospheric Measurement Techniques*, *13*(8), 4219–4245.

Rodgers, C. (2000). Inverse methods for atmospheric sounding: theory and practice. *World scientific*.

Stephens, G., Vane, D., Tanelli, S., Im, E., Durden, S., Rokey, M., ... L'Ecuyer, T. (2008). Cloudsat mission: Performance and early science after the first year of operation. *Journal of Geophysical Research: Atmospheres*, *113*(D8).

Stephens, G., & Webster, P. (1984). Cloud decoupling of the surface and planetary radiative budgets. *Journal of the Atmospheric Sciences*, *41*(4), 681–686.

Su, H., Jiang, J., Neelin, J., Shen, T., Zhai, C., Yue, Q., ... Yung, Y. (2017). Tightening of tropical ascent and high clouds key to precipitation change in a warmer climate. *Nature communications*, *8*, 15771.

Tanelli, S., Durden, S., Im, P. K., E., Reinke, D., Partain, P., Haynes, J., & Marchand, R. (2008). Cloudsat's cloud profiling radar after two years in orbit: Performance, calibration, and processing. *IEEE Transactions on Geoscience and Remote Sensing*, *46*(11), 3560–3573.

Toon, O., Starr, D., Jensen, E., Newman, P., Platnick, S., Schoeberl, M., ... Jucks, K. (2010). Planning, implementation, and first results of the tropical composition, cloud and climate coupling experiment (tc4). *Journal of Geophysical Research: Atmospheres*, *115*(D10), 3560–3573.

Zelinka, M., & Hartmann, D. (2011). The observed sensitivity of high clouds to mean surface temperature anomalies in the tropics. *Journal of Geophysical Research: Atmospheres*, *116*(D23).

Figure1.

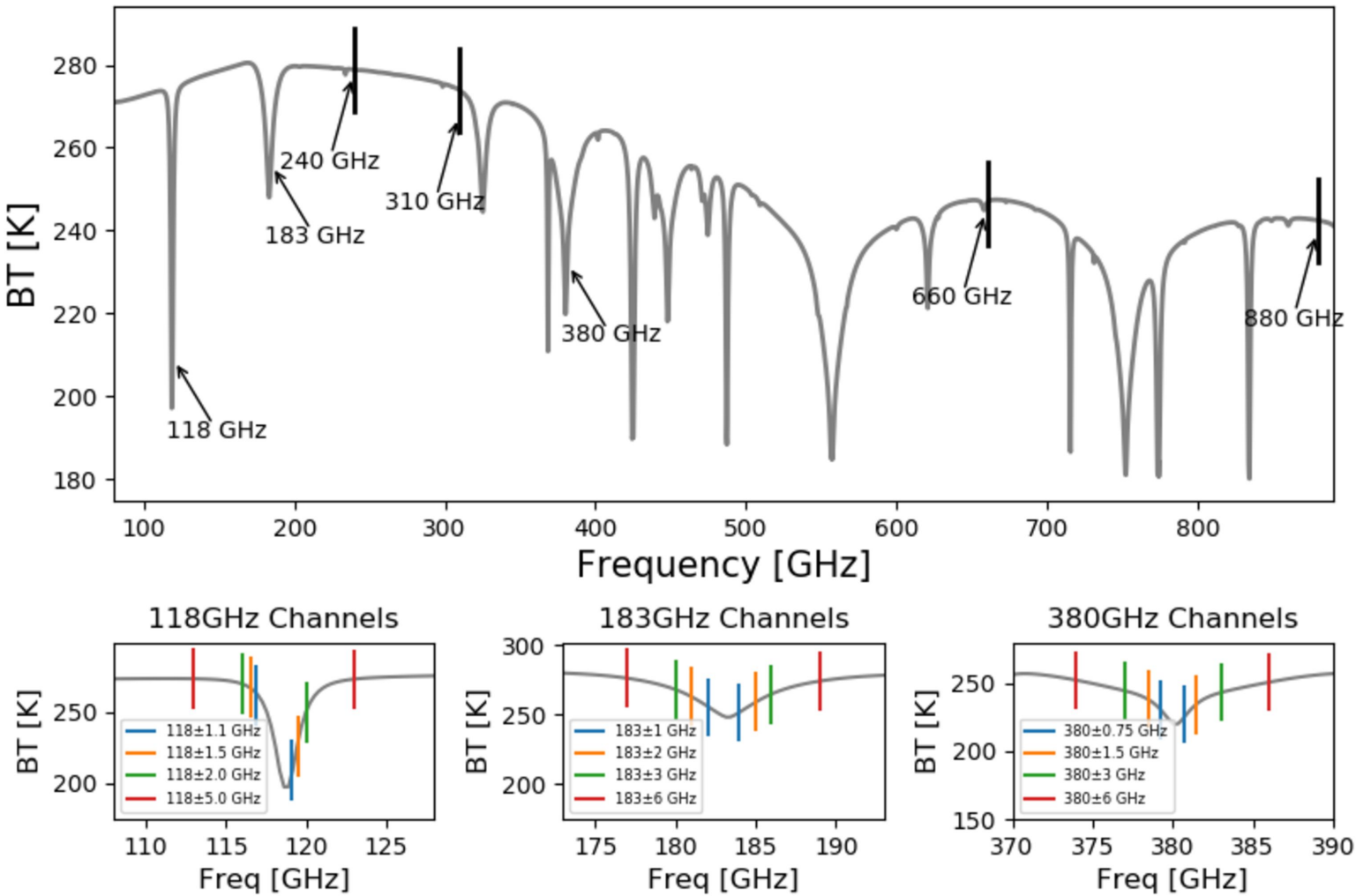
BT [K]
Frequency [GHz]
240 GHz
183 GHz
310 GHz
118 GHz
380 GHz
660 GHz
880 GHz
118GHz Channels
118±1.1 GHz
118±1.5 GHz
118±2.0 GHz
118±5.0 GHz
Freq [GHz]
183GHz Channels
183±1 GHz
183±2 GHz
183±3 GHz
183±6 GHz
380GHz Channels
380±0.75 GHz
380±1.5 GHz
380±3 GHz
380±6 GHz

Figure2.

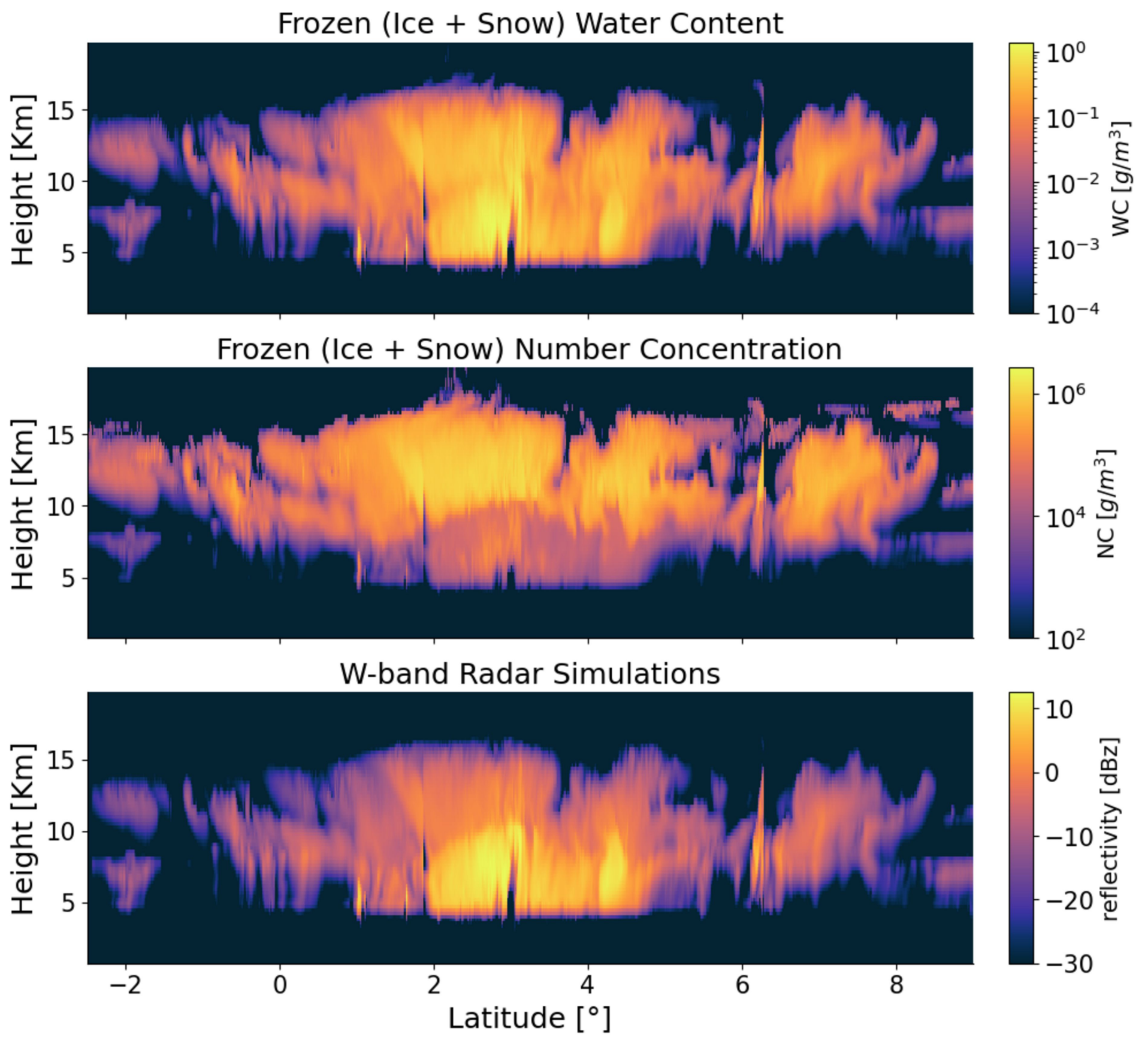
Frozen (Ice + Snow) Water Content
Height [Km]
15
10
5
10^{0}
10^{-1}
10^{-2}
10^{-3}
10^{-4}
WC [g/m^3]
Frozen (Ice + Snow) Number Concentration
Height [Km]
15
10
5
10^{6}
10^{4}
10^{2}
NC [g/m^3]
W-band Radar Simulations
Height [Km]
15
10
5
10
0
−10
−20
−30
reflectivity [dBz]
−2
0
2
4
6
8
Latitude [°]

Figure3.

Frozen Water Path

WP [g/m^2]

10^3

10^1

10^{-1}

ice water path

snow water path

118 Ghz Channels

BT [K]

260

240

118 ± 1.1 GHz

118 ± 1.5 GHz

118 ± 2.0 GHz

118 ± 5.0 GHz

183 Ghz Channels

BT [K]

275

250

225

183 ± 1.0 GHz

183 ± 2.0 GHz

183 ± 3.0 GHz

183 ± 6.0 GHz

380 Ghz Channels

BT [K]

250

200

380 ± 0.75 GHz

380 ± 1.5 GHz

380 ± 3.0 GHz

380 ± 6.0 GHz

Window Channels

BT [K]

250

200

150

240 GHz

310 GHz

660 GHz

880 GHz

−2

0

2

4

6

8

Latitude [°]

Figure4.

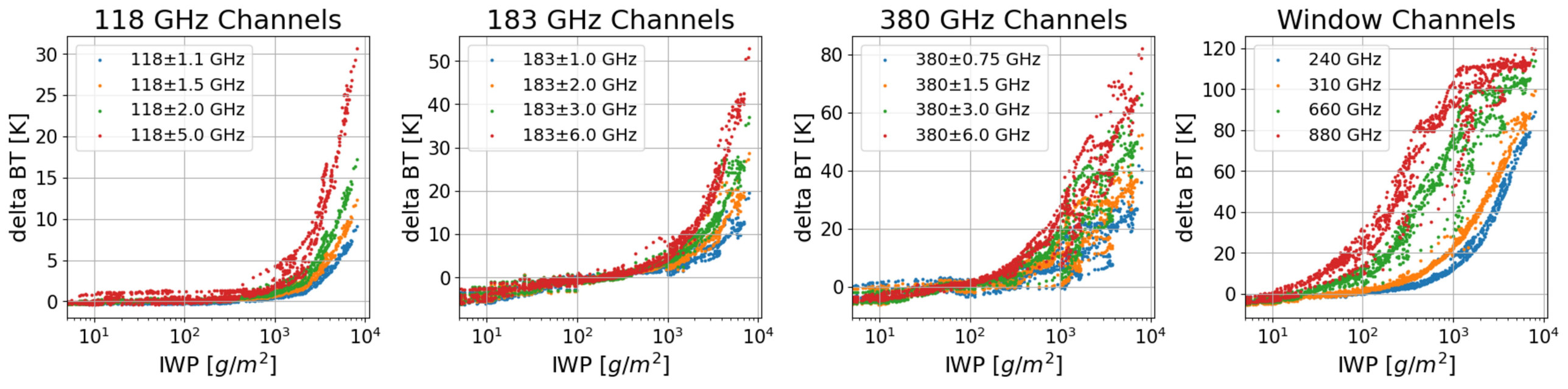
118 GHz Channels
118±1.1 GHz
118±1.5 GHz
118±2.0 GHz
118±5.0 GHz
delta BT [K]
IWP [g/m^2]
183 GHz Channels
183±1.0 GHz
183±2.0 GHz
183±3.0 GHz
183±6.0 GHz
delta BT [K]
IWP [g/m^2]
380 GHz Channels
380±0.75 GHz
380±1.5 GHz
380±3.0 GHz
380±6.0 GHz
delta BT [K]
IWP [g/m^2]
Window Channels
240 GHz
310 GHz
660 GHz
880 GHz
delta BT [K]
IWP [g/m^2]

Figure5.

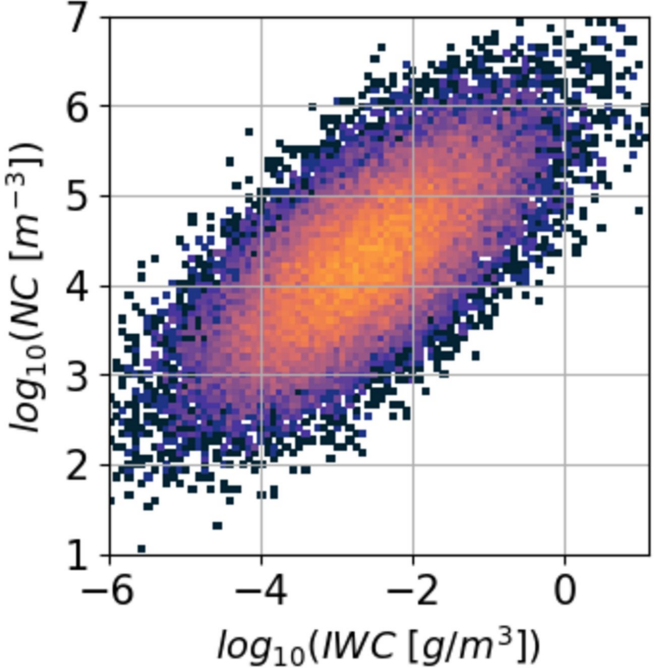
7
6
5
4
3
2
1
$log_{10}(NC\ [m^{-3}])$
−6
−4
−2
0
$log_{10}(IWC\ [g/m^3])$

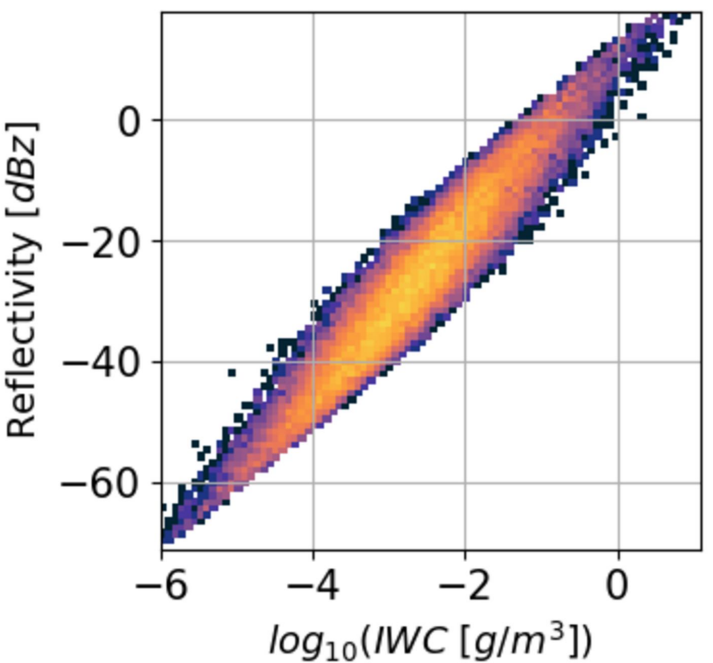
Reflectivity [dBz]
0
−20
−40
−60
−6
−4
−2
0
$log_{10}(IWC\ [g/m^3])$

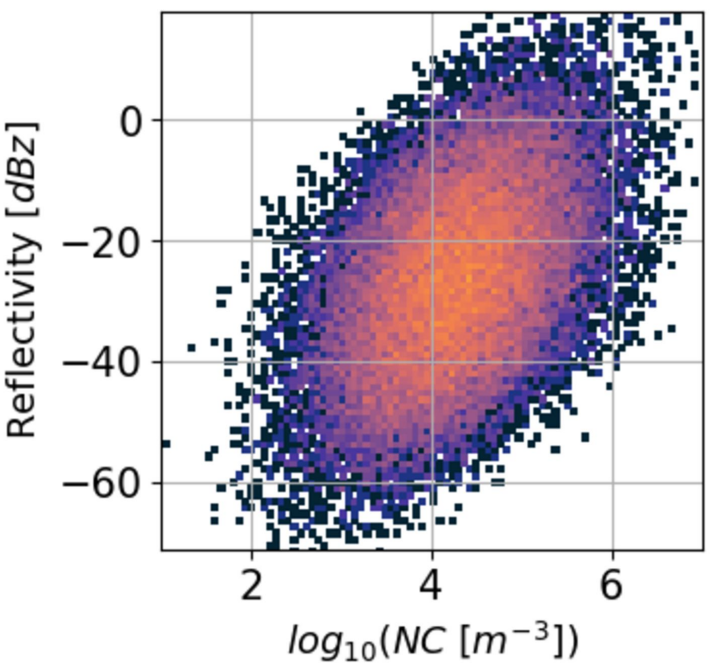
Reflectivity [dBz]
0
−20
−40
−60
2
4
6
$log_{10}(NC\ [m^{-3}])$

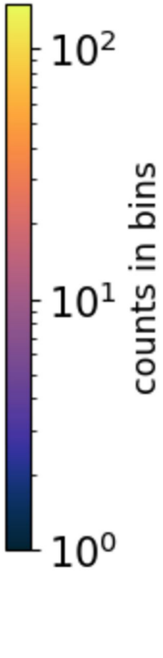
10^2
10^1
10^0
counts in bins

Figure6.

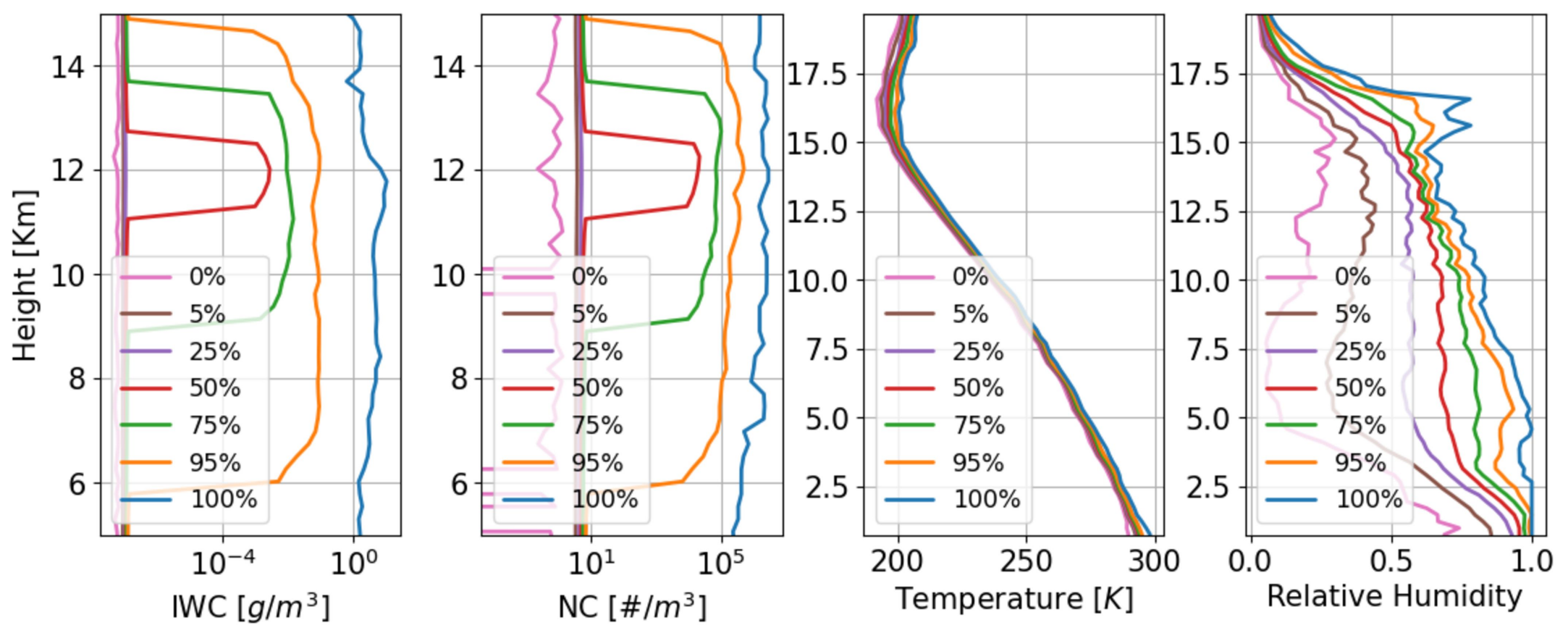
Height [Km]
IWC [g/m^3]
NC [$\#/m^3$]
Temperature [K]
Relative Humidity
0%
5%
25%
50%
75%
95%
100%

Figure7.

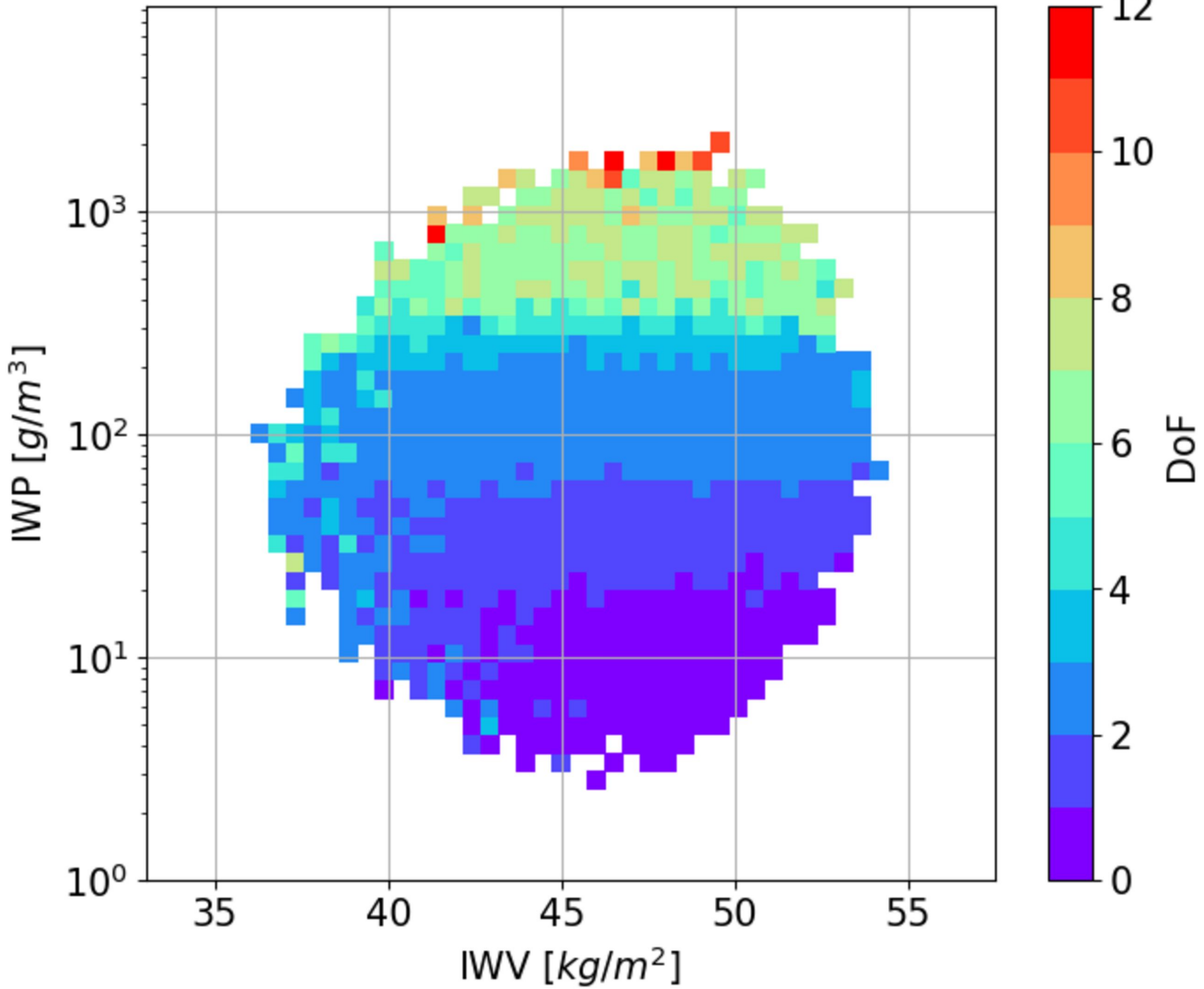
IWP [g/m^3]
10^3
10^2
10^1
10^0
35
40
45
50
55
IWV [kg/m^2]
DoF
12
10
8
6
4
2
0

Figure8.

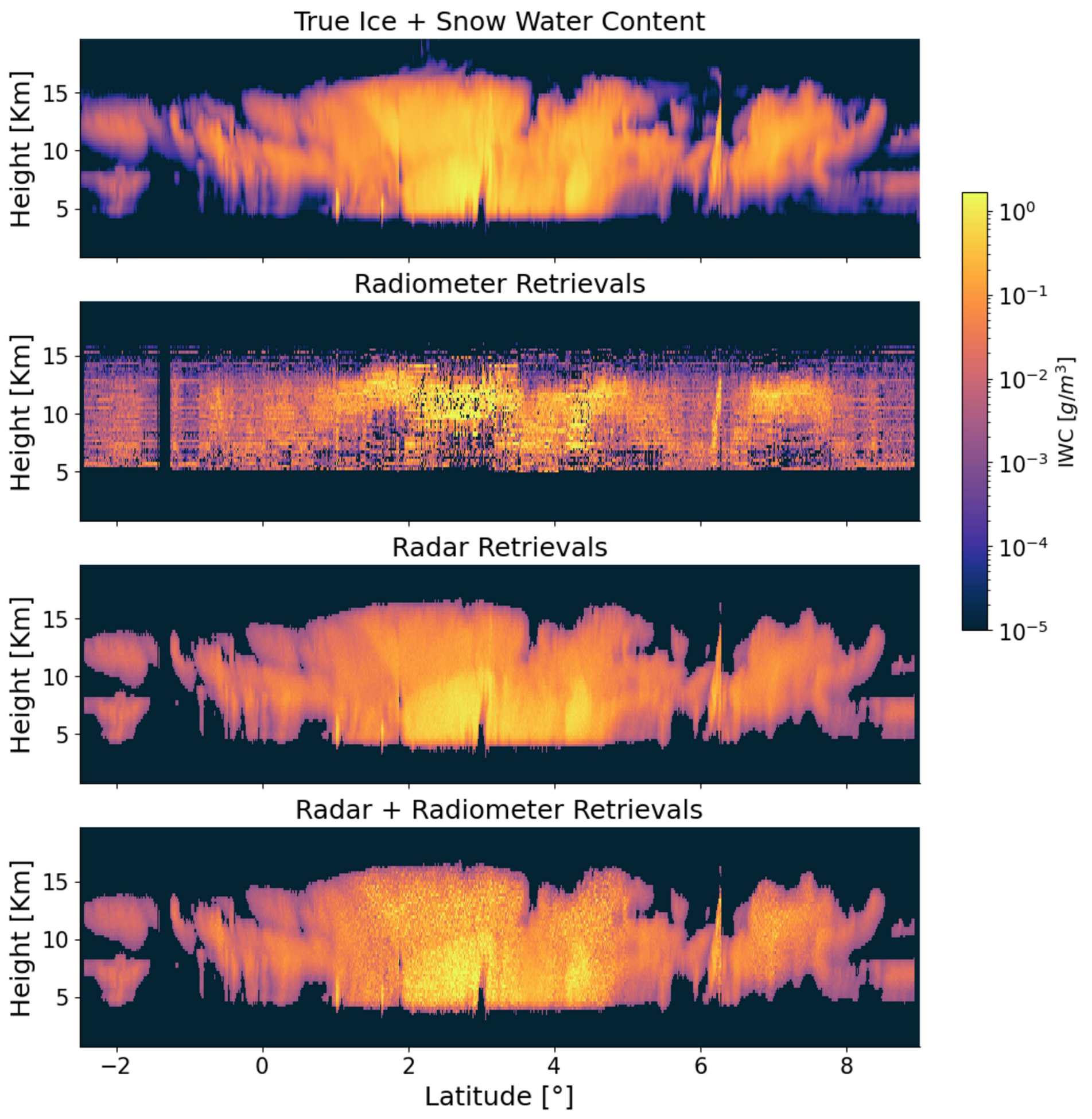
True Ice + Snow Water Content
Radiometer Retrievals
Radar Retrievals
Radar + Radiometer Retrievals
Height [Km]
15
10
5
−2
0
2
4
6
8
Latitude [°]
IWC [g/m^3]
10^0
10^{-1}
10^{-2}
10^{-3}
10^{-4}
10^{-5}

Figure9.

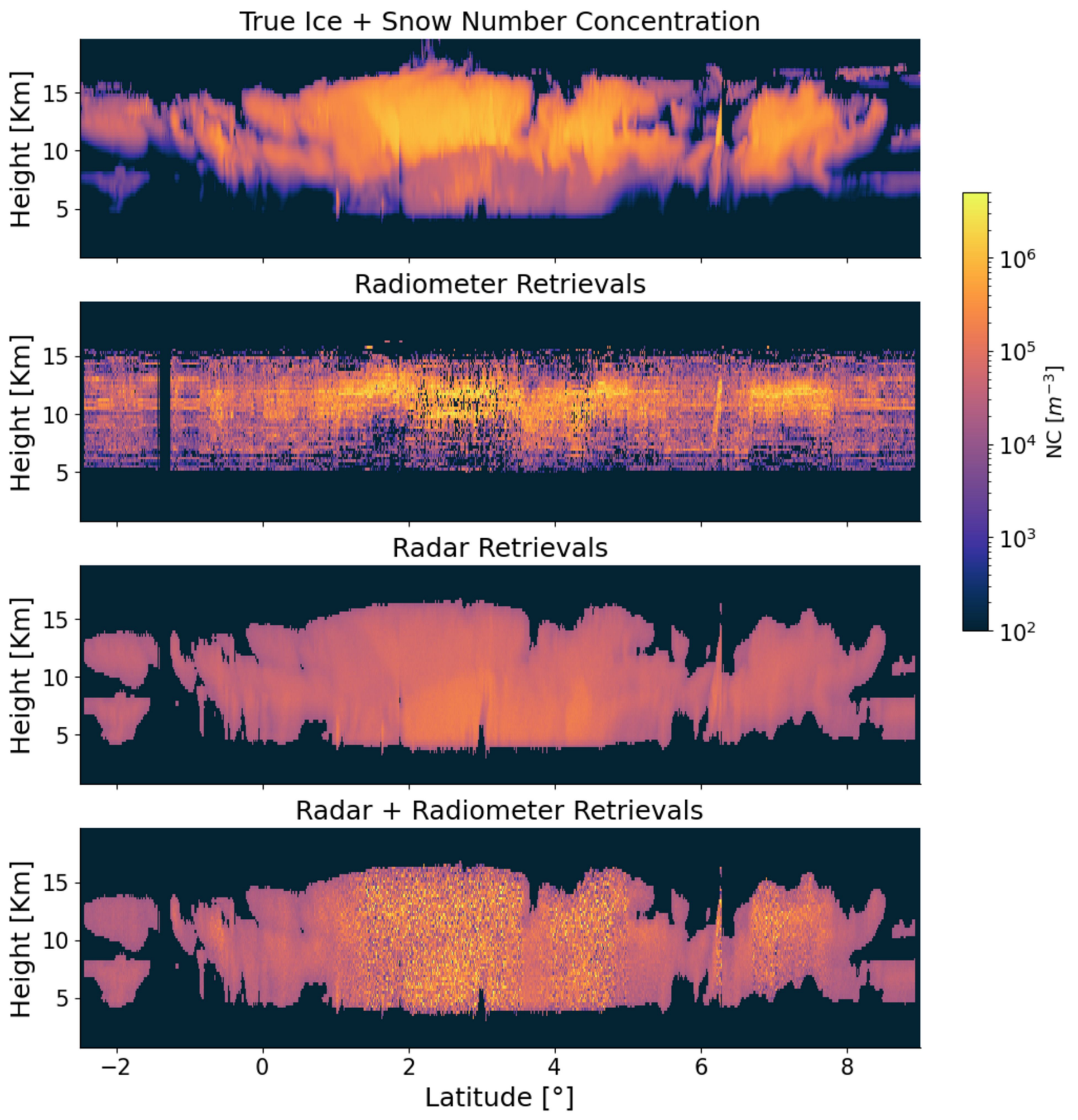
True Ice + Snow Number Concentration
Radiometer Retrievals
Radar Retrievals
Radar + Radiometer Retrievals
Height [Km]
15
10
5
−2
0
2
4
6
8
Latitude [°]
10^6
10^5
10^4
10^3
10^2
NC $[m^{-3}]$

Figure10.

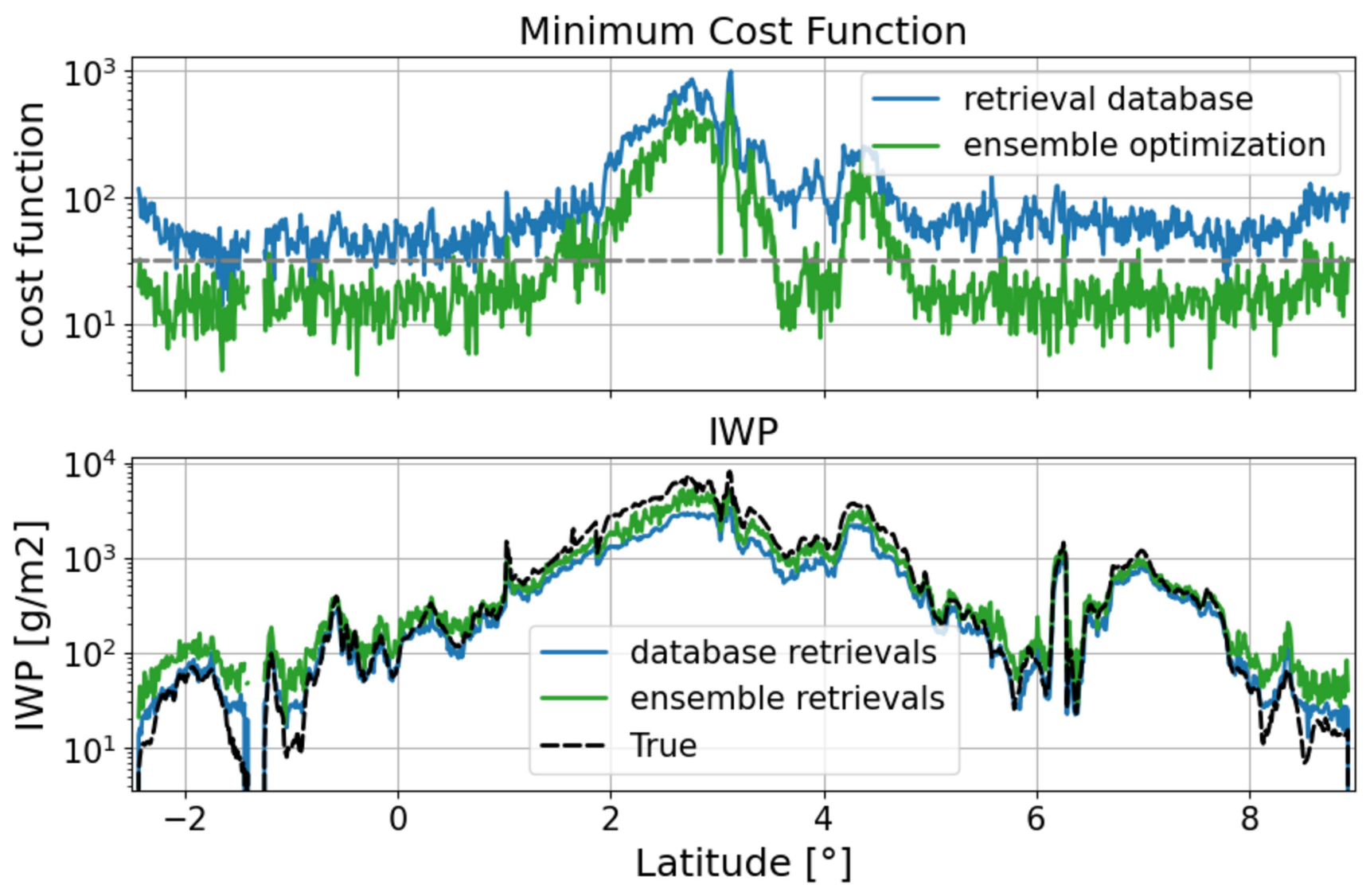
Minimum Cost Function
cost function
10^3
10^2
10^1
retrieval database
ensemble optimization
IWP
IWP [g/m2]
10^4
10^3
10^2
10^1
database retrievals
ensemble retrievals
True
−2
0
2
4
6
8
Latitude [°]

Figure11.

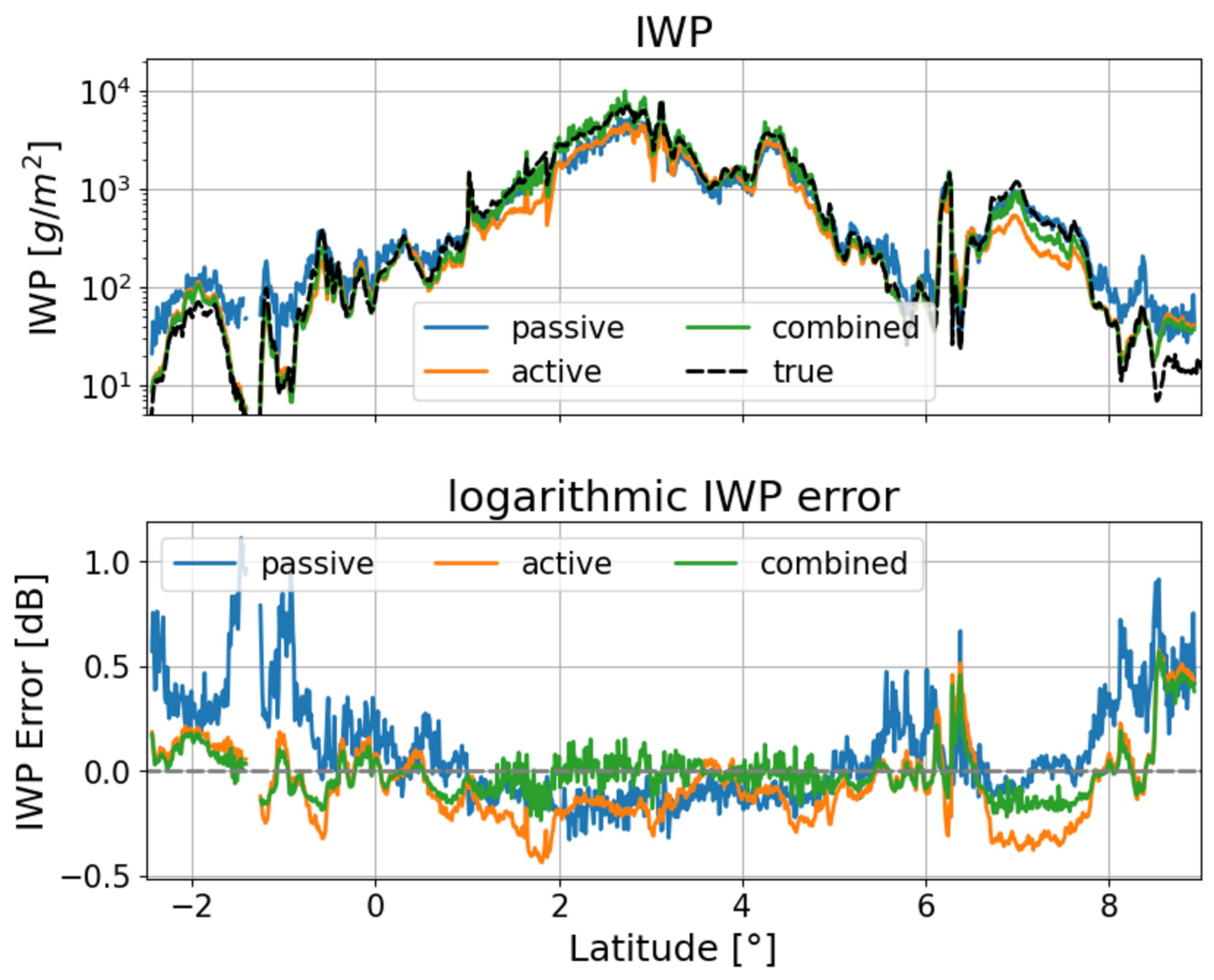
IWP
IWP [g/m^2]
10^4
10^3
10^2
10^1
passive
active
combined
true
logarithmic IWP error
IWP Error [dB]
1.0
0.5
0.0
−0.5
passive
active
combined
−2
0
2
4
6
8
Latitude [°]

Figure12.

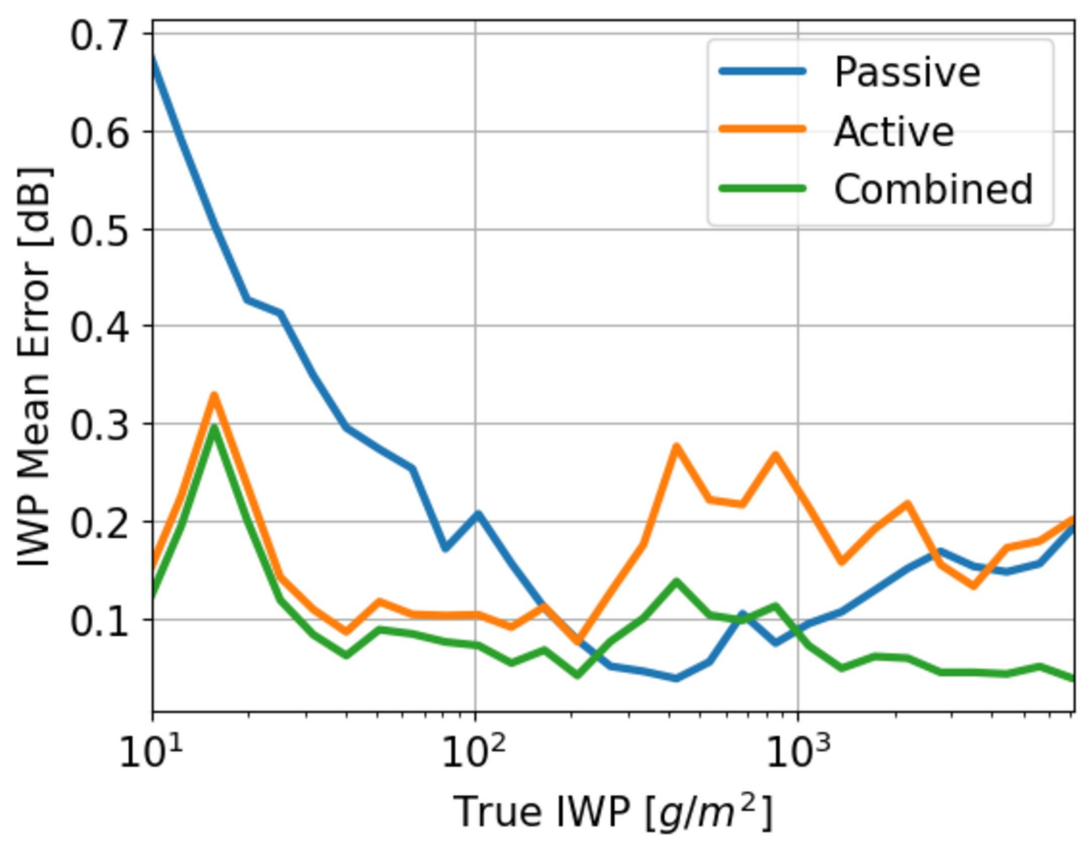
Passive
Active
Combined
IWP Mean Error [dB]
0.7
0.6
0.5
0.4
0.3
0.2
0.1
10^1
10^2
10^3
True IWP [g/m^2]

Figure13.

Radiometer

Retrieved IWC [g/m^{-3}]

True IWC [g/m^{-3}]

Radiometer

Retrieved NC [m^{-3}]

True NC [m^{-3}]

Radiometer

Retrieved IWP [g/m^{-2}]

True IWP [g/m^{-2}]

Radar

Retrieved IWC [g/m^{-3}]

True IWC [g/m^{-3}]

Radar

Retrieved NC [m^{-3}]

True NC [m^{-3}]

Radar

Retrieved IWP [g/m^{-2}]

True IWP [g/m^{-2}]

Radar + Radiometer

Retrieved IWC [g/m^{-3}]

True IWC [g/m^{-3}]

Radar + Radiometer

Retrieved NC [m^{-3}]

True NC [m^{-3}]

Radar + Radiometer

Retrieved IWP [g/m^{-2}]

True IWP [g/m^{-2}]

normalized density

Figure14.

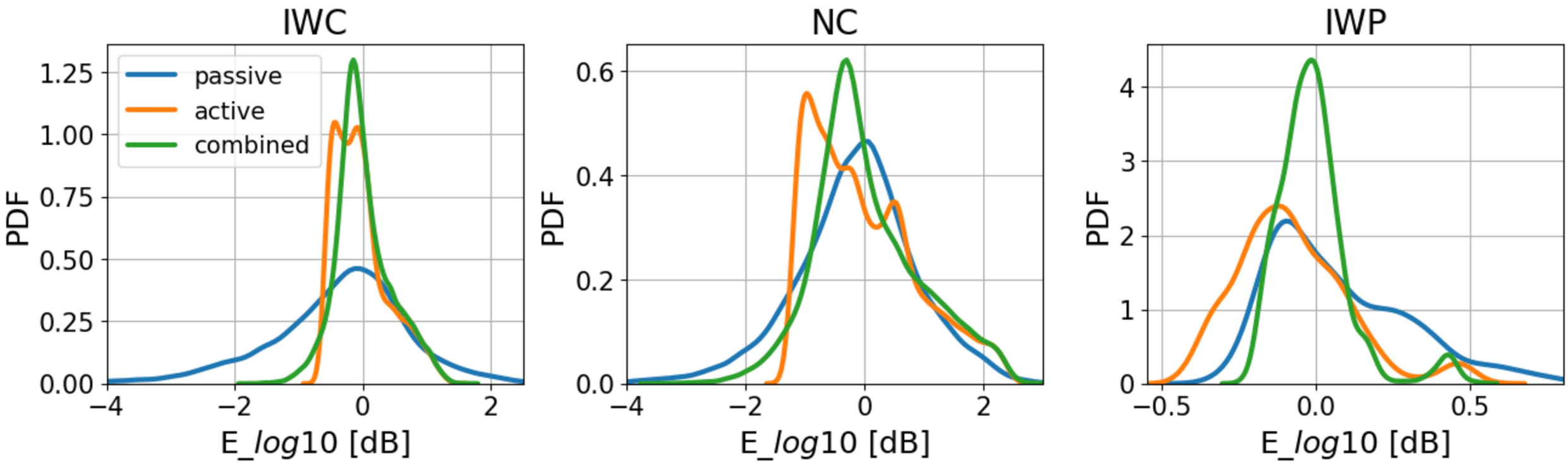
IWC
NC
IWP
passive
active
combined
PDF
E_log10 [dB]
1.25
1.00
0.75
0.50
0.25
0.00
0.6
0.4
0.2
0.0
4
3
2
1
0
−4
−2
0
2
−0.5
0.0
0.5

Figure15.

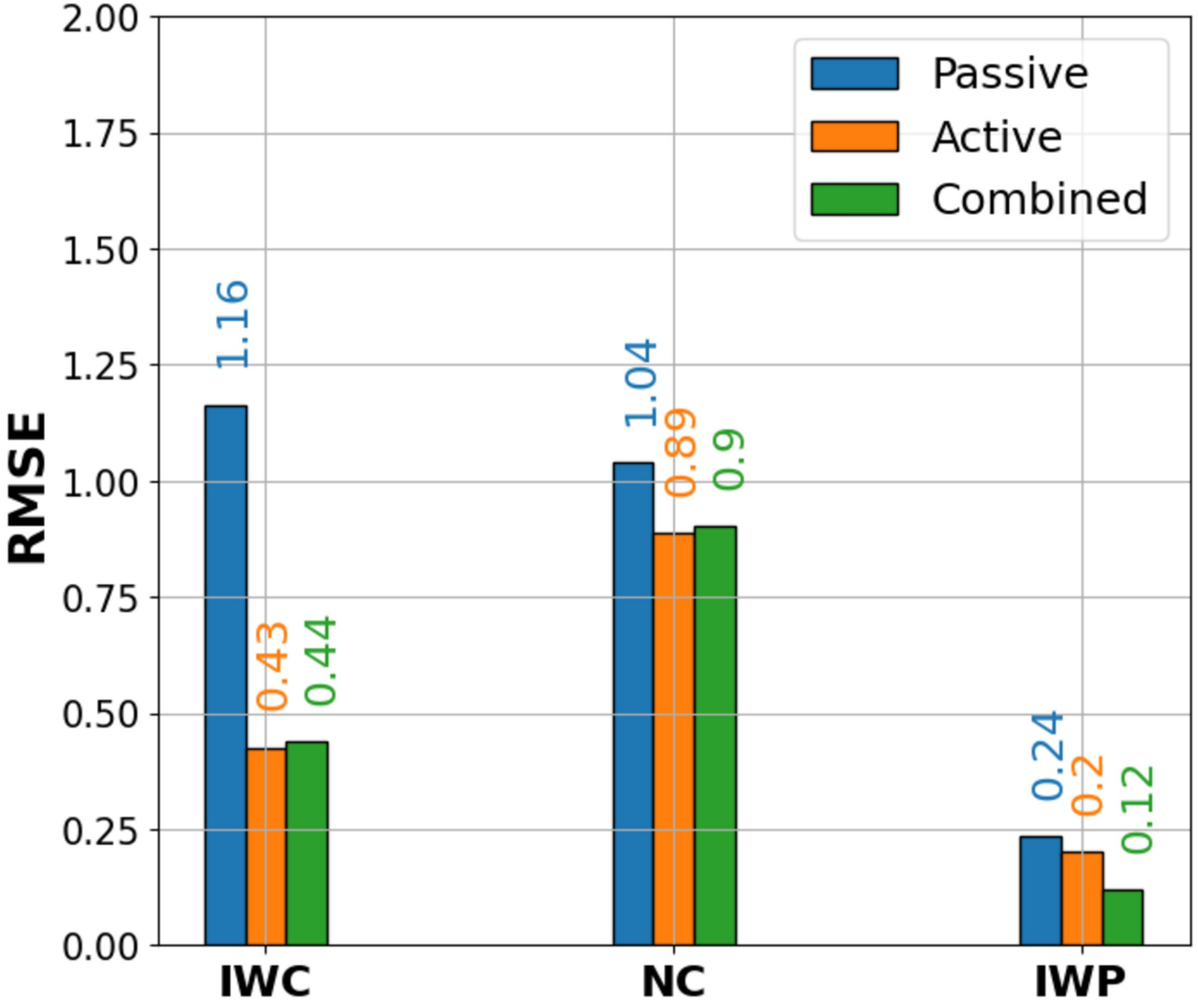
RMSE
2.00
1.75
1.50
1.25
1.00
0.75
0.50
0.25
0.00
Passive
Active
Combined
1.16
0.43
0.44
1.04
0.89
0.9
0.24
0.2
0.12
IWC
NC
IWP

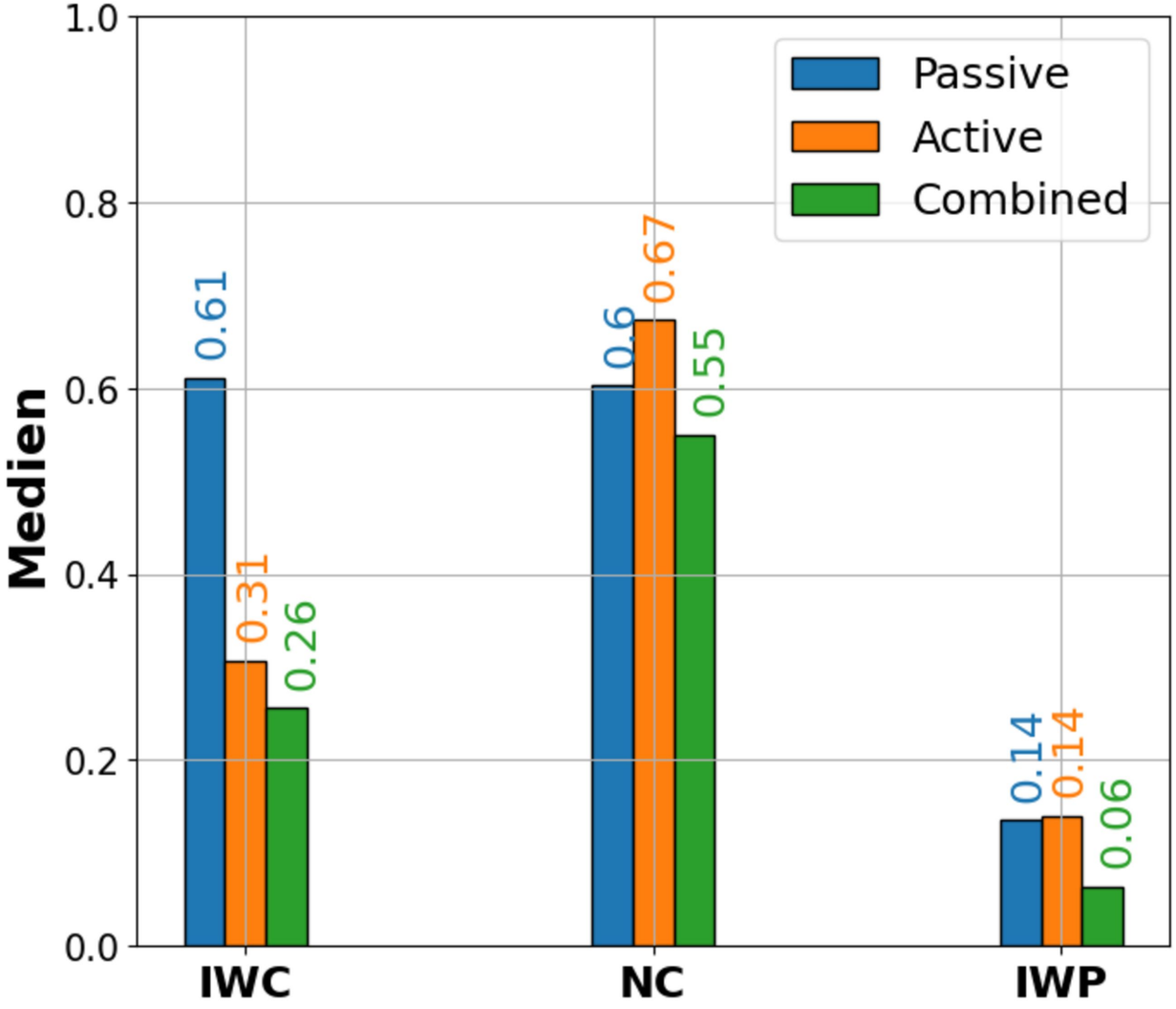
Medien
1.0
0.8
0.6
0.4
0.2
0.0
Passive
Active
Combined
0.61
0.31
0.26
0.6
0.67
0.55
0.14
0.14
0.06
IWC
NC
IWP